C. elegans molting requires rhythmic accumulation of the Grainyhead/LSF transcription factor GRH-1

Milou W M Meeuse[1,2] , Yannick P Hauser[1,2] , Smita Nahar[1] , A Alexander T Smith[1] , Kathrin Braun[1] , Chiara Azzi[1,2] , Markus Rempfler[1] & Helge Großhans[1,2,*]

Abstract

C. elegans develops through four larval stages that are rhythmically terminated by molts, that is, the synthesis and shedding of a cuticular exoskeleton. Each larval cycle involves rhythmic accumulation of thousands of transcripts, which we show here relies on rhythmic transcription. To uncover the responsible gene regulatory networks (GRNs), we screened for transcription factors that promote progression through the larval stages and identified GRH-1, BLMP-1, NHR-23, NHR-25, MYRF-1, and BED-3. We further characterize GRH-1, a Grainyhead/LSF transcription factor, whose orthologues in other animals are key epithelial cell-fate regulators. We find that GRH-1 depletion extends molt durations, impairs cuticle integrity and shedding, and causes larval death. GRH-1 is required for, and accumulates prior to, each molt, and preferentially binds to the promoters of genes expressed during this time window. Binding to the promoters of additional genes identified in our screen furthermore suggests that we have identified components of a core molting-clock GRN. Since the mammalian orthologues of GRH-1, BLMP-1 and NHR-23, have been implicated in rhythmic homeostatic skin regeneration in mouse, the mechanisms underlying rhythmic *C. elegans* molting may apply beyond nematodes.

Introduction

C. elegans larval development subdivides into four larval stages, each terminated by a molt. In the first step of the molt, termed apolysis, the connections of the existing cuticle to the underlying epidermis are severed. Subsequently, a new cuticle is synthesized, before the old cuticle is shed in a final step termed ecdysis. Traditionally, the time of molting is equated with lethargus, a period of relative behavioral quiescence, when animals stop feeding. For simplicity, we will follow this tradition here but note that additional events required for successful molting precede lethargus (Cohen *et al*, 2020; Cohen & Sundaram, 2020; Tsiairis & Großhans, 2021).

Molts occur at regular intervals of 7–8 h at 25°C, and a clock-type mechanism has been invoked to explain this regularity (Monsalve & Frand, 2012; Tsiairis & Großhans, 2021). Such a clock mechanism may also explain, and be partially based on, the rhythmic expression of thousands of genes that is coupled to the molting cycle (Kim *et al*, 2013; Hendriks *et al*, 2014; Turek & Bringmann, 2014; Meeuse *et al*, 2020). However, the components of this clock, and accordingly their wiring, have remained largely elusive (Tsiairis & Großhans, 2021).

Counter-intuitively, rhythmic mRNA accumulation in the mammalian circadian clock appears to rely chiefly on co- and post-transcriptional mechanisms, including rhythmic splicing (Koike *et al*, 2012; Menet *et al*, 2012; Preußner *et al*, 2017). Here, we demonstrate that transcript-level oscillations in *C. elegans* larvae are parsimoniously explained by rhythmic RNA polymerase II recruitment to promoters. This finding suggests that rhythmically active transcription factors are components of the underlying machinery, or core oscillator, and thus presumably also the molting cycle clock. To identify possible candidates, we screened through a selection of rhythmically expressed transcription factors, assuming that rhythmic transcription would be a possible (though not necessarily the only) mechanism of achieving rhythmic transcription factor activity. From a set of 92 such transcription factors (Hendriks *et al*, 2014), we identified six whose depletion altered molt number and/or duration. These include the nuclear hormone receptors NHR-23 and NHR-25 and the myelin regulatory family transcription factor MYRF-1/PQN-47, which had previously been linked to molting (Kostrouchova *et al*, 1998, 2001; Gissendanner & Sluder, 2000; Gissendanner *et al*, 2004; Frand *et al*, 2005; Russel *et al*, 2011; Meng *et al*, 2017; preprint: Johnson *et al*, 2021), as well as novel factors.

We characterize the function of GRH-1, the sole *C. elegans* member of the phylogenetically conserved LSF/Grainyhead family (Venkatesan *et al*, 2003). Grainyhead proteins are key regulators of differentiation, maintenance, integrity, and repair of different epithelial tissues in animals (Sundararajan *et al*, 2020). RNAi-mediated

1 Friedrich Miescher Institute for Biomedical Research (FMI), Basel, Switzerland
2 University of Basel, Basel, Switzerland
   *Corresponding author. Tel: +41 61 697 66 51; E-mail: helge.grosshans@fmi.ch

depletion of *C. elegans* GRH-1 causes embryonic death, potentially due to cuticular defects (Venkatesan *et al*, 2003). We report that post-embryonically, GRH-1 accumulates rhythmically and promotes molting through its activity in a specific window during each larval stage. Its depletion delays the onset of ecdysis in a dose-dependent manner, to the point that animals severely depleted arrest development and die. Finally, we find that endogenous GRH-1 binds to the promoters of additional screen hits.

Our results, together with the validation of an additional hit, BLMP-1, in separate work by us and others (preprint: Hauser *et al*, 2021; Stec *et al*, 2021; Stojanovski *et al*, 2022), provide new insights into the transcriptional mechanisms that support rhythmic molting and identify potential molting clock components. The fact that orthologues of GRH-1, as well as of additional screen hits, also function in rhythmic homeostatic skin regeneration in mouse (Steinmayr *et al*, 1998; Magnusdottir *et al*, 2007; Wilanowski *et al*, 2008; Telerman *et al*, 2017), suggests mechanistic similarities between this process and the molting process of nematodes.

Results

Rhythmic transcription of oscillating genes is driven by rhythmic RNA polymerase II occupancy

Previous observations that the levels of intronic RNA encoded by oscillating genes also oscillate (Hendriks *et al*, 2014) provided circumstantial evidence for a model of rhythmic gene transcription. However, technical limitations restricted this analysis to a set of highly expressed genes with long introns, and genuine pre-mRNAs could not be distinguished from excised introns. Hence, we employed temporally resolved DNA-dependent RNA polymerase II (RNAPII) chromatin immunoprecipitation coupled to sequencing (ChIP-seq) to examine the dynamics of RNAPII binding to oscillating gene promoters. We used a population of synchronized wild-type worms collected hourly from 22 h until 33 h of post-embryonic development at 25°C and quantified a 1-kb window around the transcription start sites (TSSs) as a proxy for temporal RNAPII promoter occupancy on annotated oscillating genes (Meeuse *et al*, 2020). As a reference, we quantified mRNA levels on the same samples using RNA sequencing. This revealed widespread rhythmic binding of RNAPII at the promoters of oscillating genes (Figs 1A–C and EV1A, Dataset EV1).

We also detected instances where oscillating mRNA levels were not accompanied by rhythmic RNAPII promoter binding. It is possible that this might reflect cases of post-transcriptional regulation. However, we consider it more likely a technical artifact, because we noticed a general reduction of amplitudes in the ChIP-sequencing relative to the RNA-sequencing experiment, probably reflecting a reduced sensitivity and dynamic range of the former over the latter. Indeed, oscillating genes for which we observed a positive correlation between RNAPII occupancy and mRNA expression tended to be more highly expressed and to exhibit a higher amplitude than other oscillating genes (Fig EV1B–D). This limitation notwithstanding, the data support the notion that rhythmic transcription is a major contributor to rhythmic transcript accumulation and specifically point to rhythmic recruitment of RNAPII as a relevant mechanism.

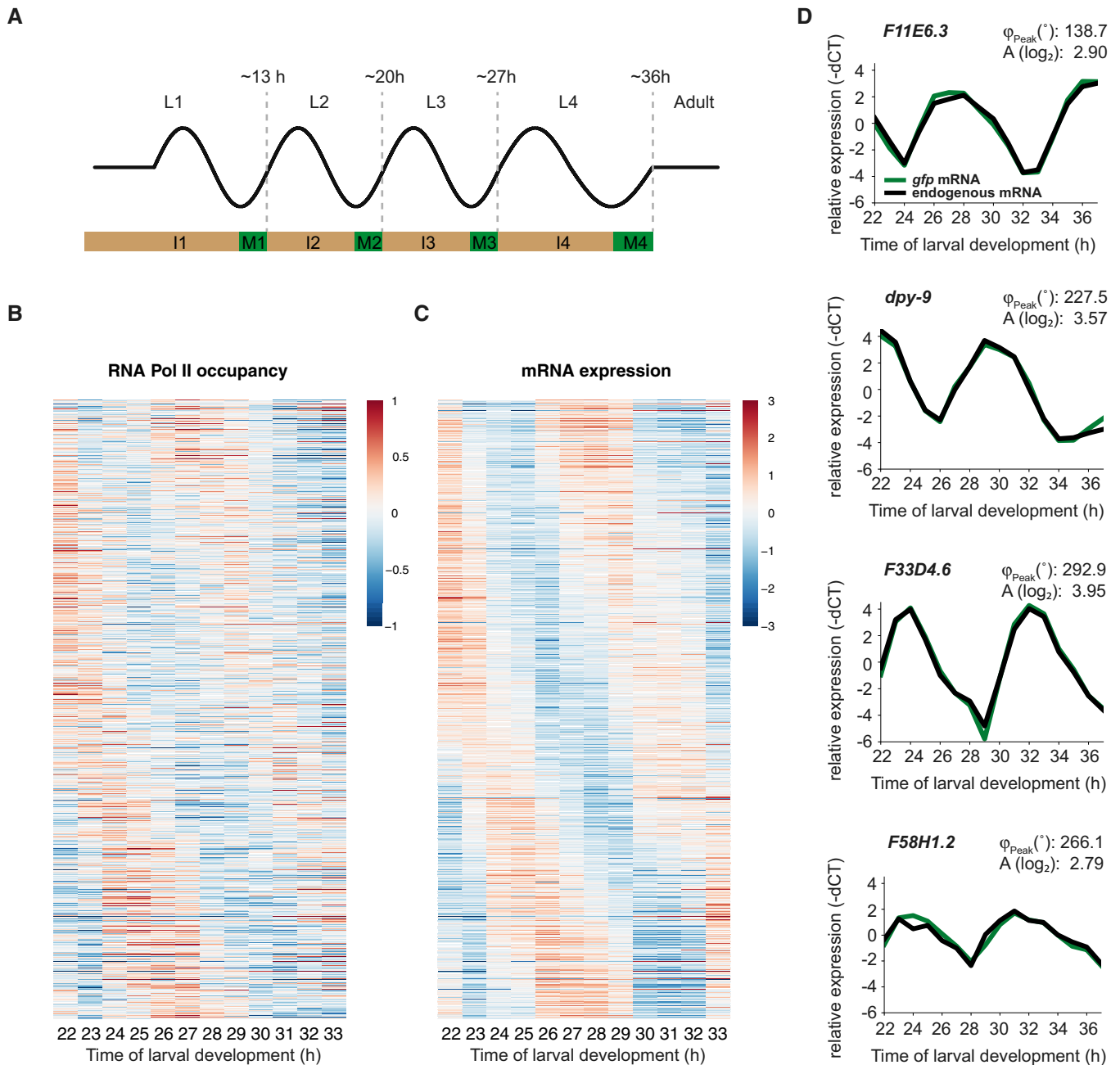## Promoter-driven *gfp* reporter transgenes recapitulate transcription of endogenous genes

To understand in more detail how rhythmic transcription drives mRNA level oscillations, we characterized transcriptional reporters that contained the putative promoters (either 2 kb upstream of the ATG or until the next upstream gene) of oscillating genes fused to a sequence encoding destabilized, nucleus-localized green fluorescent protein (GFP). We chose promoters from genes with a variety of peak expression phases and amplitudes. To exclude 3′UTR-mediated posttranscriptional regulation, the reporters further contained the *unc-54* 3′UTR, which we selected because *unc-54* did not display transcript level oscillation in our mRNA sequencing time courses (Hendriks *et al*, 2014; Meeuse *et al*, 2020) and because its 3′UTR appears devoid of regulatory activity (Brancati & Großhans, 2018). All reporters were integrated into the *C. elegans* genome in single copy at the same defined genomic locus.

To assess the extent to which transgenes, and thus promoter activity, could recapitulate endogenous rhythmic gene activity, we compared dynamic changes in abundance of the endogenous transcript and its *gfp* mRNA counterpart within the same worm lysates of synchronized worm populations over time. Specifically, we plated starved L1 larvae on food at 25°C and sampled hourly between 22–37 h after plating (Figs 1D and EV2A). In each of the eight cases that we examined, we observed rhythmic reporter transcript accumulation. Remarkably, the patterns of the endogenous transcripts and their derived reporters were highly similar, that is, in all tested cases except one, peak phases and amplitudes were comparable (Figs 1D and EV2A). (We suspect that in the one case where we observe a deviation, *R12.E2.7p* in Fig EV2A, the reporter may lack relevant promoter or intronic enhancer elements, but we have not ruled out posttranscriptional regulation.) Furthermore, in the case of *F58H1.2*, the reporter RT-qPCR time course recapitulated high-amplitude oscillations despite a much more modest oscillatory signal in the ChIP-seq experiment (Fig EV2B), further supporting the notion that the differences in amplitudes between ChIP-seq and mRNA-seq probably are of technical nature and do not primarily arise from post-transcriptional regulation of the transcripts.

Taken together, these results reveal that the promoters of a variety of oscillating genes are sufficient to recapitulate endogenous transcript dynamics.

A targeted screen identifies transcription factors involved in molting

Prompted by the above findings, we sought to identify rhythmically active transcription factors involved in molting. Hence, we performed an RNAi screen targeting 92 transcription factors that exhibit transcript level oscillations according to our previous annotation (Hendriks *et al*, 2014). Specifically, we screened for aberrant developmental progression or molt execution. To obtain such information, we examined luciferase activity in animals that express a luciferase transgene constitutively from the *eft-3* promoter and that are grown in the presence of D-luciferin (Olmedo *et al*, 2015; Meeuse *et al*, 2020). This assay detects lethargus by a drop in luminescence at the level of individual animals, allowing us to quantify durations of molts, intermolts and, as a sum of the two, entire larval stages for many animals per condition. We depleted the

A

B

RNA Pol II occupancy

Time of larval development (h)

C

mRNA expression

Time of larval development (h)

D

F11E6.3 $\varphi_{Peak}(°)$: 138.7   A ($\log_2$): 2.90

dpy-9 $\varphi_{Peak}(°)$: 227.5   A ($\log_2$): 3.57

F33D4.6 $\varphi_{Peak}(°)$: 292.9   A ($\log_2$): 3.95

F58H1.2 $\varphi_{Peak}(°)$: 266.1   A ($\log_2$): 2.79

Figure 1. Oscillatory gene expression arises from promoter-driven rhythmic transcription.

A   Schematic of *C. elegans* larval development and oscillatory gene expression. Intermolts (I), Molts (M) and larval stages with their approximate durations at 25°C (based on Meeuse *et al*, 2020) are indicated. Note that other oscillating genes will differ in peak phase, but not period, from the indicated example.

B, C $\log_2$-transformed, mean-normalized RNA polymerase II ChIP (B) and RNA (C) sequencing reads of all 3,739 previously defined oscillating genes (Meeuse *et al*, 2020) ordered according to the published peak phase. For clarity, values are capped at absolute values of 1 (B) and 3 (C), respectively, and plotted across samples; color keys indicate $\log_2$ fold changes.

D   RT-qPCR time courses. Promoters of the indicated oscillating genes were used to drive expression of a destabilized, nuclear GFP protein from a single copy integrated transgene; *gfp* mRNA and the endogenous transcript driven by the same promoter were quantified from the same RNA samples. Relative expression was calculated as −dCT = − (target CT values − actin CT values) and then mean normalized for each trace individually. Peak phases (ϕ_{Peak}) and amplitudes (A) for the endogenous transcripts are from (Meeuse *et al*, 2020). qPCR was performed in technical replicate, shown are averages.

Data information: These and all other experiments were performed once unless indicated otherwise. See also Figs EV1 and EV2, Dataset EV1.

transcription factors by feeding animals RNAi-expressing bacteria. To control for differences in larval growth among RNAi conditions unrelated to target protein depletion, we performed the experiment in parallel on RNAi deficient *rde-1(ne219)* mutant animals (Tabara *et al*, 1999) (Fig 2A).

By plotting the luminescence intensities sorted by entry into the first molt in a heatmap (Fig 2B and C), we identified six genes whose depletion caused an apparent arrest in development or death, often following extended lethargic periods (*nhr-23*, *myrf-1*, and *grh-1*; Fig 2B and D, Appendix Fig S1), or aberrant duration of molts (*bed-3*, *blmp-1*, and *nhr-25*; Figs 2C and D, and EV3).

The nuclear hormone receptors NHR-23 and NHR-25 have previously been shown to function in molting (Kostrouchova *et al*, 1998, 2001; Gissendanner & Sluder, 2000; Gissendanner *et al*, 2004; Frand *et al*, 2005; preprint: Johnson *et al*, 2021), and we and others have recently described functions of BLMP-1 in oscillatory gene expression and cuticle formation (preprint: Hauser *et al*, 2021; Sandhu *et al*, 2021; Stec *et al*, 2021; Stojanovski *et al*, 2022). Here, we sought to characterize GRH-1, whose orthologues are key regulators of epithelial cell fates and remodeling of epithelial tissues in other animals (Sundararajan *et al*, 2020), and which had no known role in *C. elegans* post-embryonic development.

Loss of GRH-1 results in abnormal ecdysis and larval death

Injection of double-stranded RNA targeting *grh-1* into the germline of L4 stage larval animals causes embryonic lethality in the next generation (Venkatesan *et al*, 2003). To bypass this defect and investigate the role of GRH-1 during larval development, we performed controlled GRH-1 depletion in larvae using the auxin-inducible degradation (AID) system (Zhang *et al*, 2015). We tagged *grh-1* endogenously with *aid::3xflag* to generate allele *grh-1(xe135)*, and expressed the plant-specific F-box protein TIR1 from a transgene, generating a strain that, for simplicity's sake, we will refer to as *grh-1::aid* in the following.

When we placed synchronized L1 stage *grh-1::aid* animals on 1 mM auxin-containing plates, we observed that 24 h after plating, 41% (207/500) of animals had died during an abnormal ecdysis. Surviving animals were variably sized but generally much smaller than wild-type control animals (which were ~ L3), and subsequently also succumbed to failed ecdysis. Thus, GRH-1 depletion caused fully penetrant lethality with no viable larvae left on plate by 38 h.

To study the molting process in greater detail, we used time-lapse DIC imaging to observe L1 animals transferred to an agar pad in a drop of M9 buffer, which allowed them to move. We could readily identify loosened cuticles at the tip of the head in both wild-type and GRH-1-depleted animal (Fig 3A and B). Next, animals made spontaneous back-and-forth movements and the pharynx contracted rapidly (Movies EV1 and EV2), after which wild-type animals shed the cuticle (ecdysed) (Fig 3A and B). By contrast, in GRH-1-depleted animals, the cuticle became even looser and more inflated in the head region (Fig 3C). Vesicles appeared in the cavity underneath the loosened cuticle (Fig 3C). Finally, the cuticle broke in the head region and the underlying tissue was extruded (Fig 3C, Movie EV3). This phenotype partially resembles that of NHR-23-depleted and MYRF-1-depleted animals, both of which fail to properly shed the cuticle, but do not explode (Kostrouchova *et al*, 1998; preprint: Johnson *et al*, 2021 and our unpublished data). Cuticle

rupturing during ecdysis also provides a likely explanation for the abnormal traces observed for GRH-1-depleted animals in the luciferase assay (Appendix Fig S1). Indeed, *nlp-29*, a previously described sensor of cuticle integrity (Pujol *et al*, 2008; preprint: Johnson *et al*, 2021), was expressed at inappropriately high levels in *grh-1* RNAi-treated animals, prior to bursting (Appendix Fig S2). Moreover, and consistent with a defective cuticular barrier in *grh-1::aid* animals at low auxin levels that do not cause lethality (see below), luminescence was increased during lethargus, when animals do not ingest luciferin (Appendix Fig S2). We conclude that GRH-1 is required for viability at least in part through its role in proper cuticle formation and/or barrier function.

### Moderate GRH-1 depletion extends molt durations

We noted an increased duration of molts before GRH-1-depleted animals died (Fig 2B, see also Figs 5 and 7B below). To examine this phenotype further, we exposed *grh-1::aid* animals to varying auxin concentrations to titrate GRH-1 depletion. To avoid non-specific effects of auxin concentrations exceeding 1 mM (Appendix Fig S3), we used lower concentrations, ranging from 1 mM down to 61 nM. Auxin concentrations of ≥975 nM at hatching yielded a fully penetrant M1 phenotype (Appendix Fig S4A). Further titrations revealed that below 400 nM, an increasing fraction of animals completed additional molts (Fig 4A, Appendix Fig S4A). We quantified the developmental tempo for animals that, at the lowest auxin concentrations tested (53 nM, 79 nM, and 119 nM), completed the first three molts. We observed a specific, dose-dependent lengthening in M1, M2, and M3 (Fig 4B, Appendix Fig S4C). This effect increased with each molt. By contrast, little or no change occurred for the duration of the intermolts preceding the lengthened molts (Fig 4C, Appendix Fig S4B). Hence, whereas extensive GRH-1 depletion results in a dysfunctional cuticle and larval death, more modest perturbations change molt durations quantitatively.

GRH-1 is repetitively required for each molt

We predicted that a component of the core molting machinery would be required for each of the four larval molts, distinguishing it from stage-specific factors that are relevant to individual molts only. To test such a general role of GRH-1, we depleted GRH-1 at different stages of development through timed application of auxin. Recapitulating the effect of auxin application to synchronized L1 stage animals grown on a plate, application of auxin at hatch prevented animals from developing beyond M1 (Fig 5A). Moreover, when we applied auxin at the beginning of the L2, L3, and L4 stage, respectively, this prevented animals from developing beyond the next respective molt, that is, M2, M3, and M4 (Fig 5B–D). All these effects were fully penetrant when scored on ≥19 animals. We conclude that GRH-1 is repetitively required during development, for successful completion of each molt. Moreover, defects occur within the stage in which GRH-1 is depleted.

### GRH-1 protein levels oscillate and peak shortly before molt entry

Since GRH-1 is required repetitively, for proper execution of each of the four molts, and its mRNA levels oscillate (Hendriks *et al*, 2014; Meeuse *et al*, 2020), we wondered whether GRH-1 protein
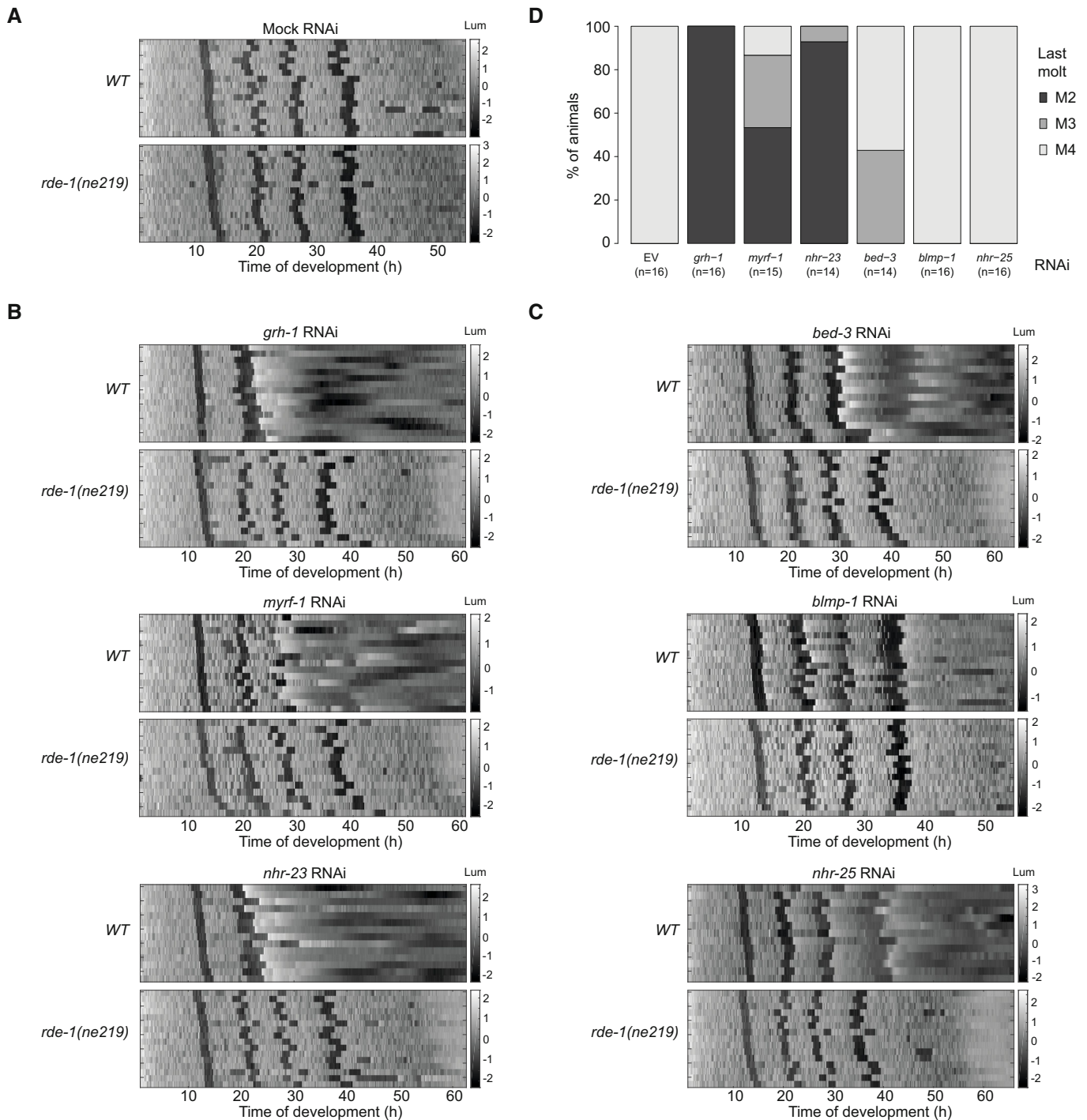
Figure 2. An RNAi screen identifies transcription factors required for normal progression through larval molting cycles.

A   Heatmap showing trend-corrected luminescence (Lum) of wild-type (*WT*, strain HW1939, top) and RNAi-deficient (*rde-1(ne219)*, strain HW2150, bottom) animals expressing luciferase from the *eft-3* promoter grown on mock (empty vector L4440) RNAi in a temperature-controlled incubator set to 20°C. Each line represents one animal. Hatch is set to *t* = 0 h and traces are sorted by entry into the first molt. Darker color corresponds to low luminescence and is associated with the molt.

B, C   Heatmap showing trend-corrected luminescence as in (A), for indicated RNAi conditions causing altered numbers (B) or durations (C) of molts, respectively.

D   Quantification of the percentage of animals entering specific molts on indicated RNAi conditions. Shown are the last molts observed for animals in each condition; for example, 100% of GRH-1 depleted fail to progress beyond M2.

Data information: See also Fig EV3, Appendix Fig S1.
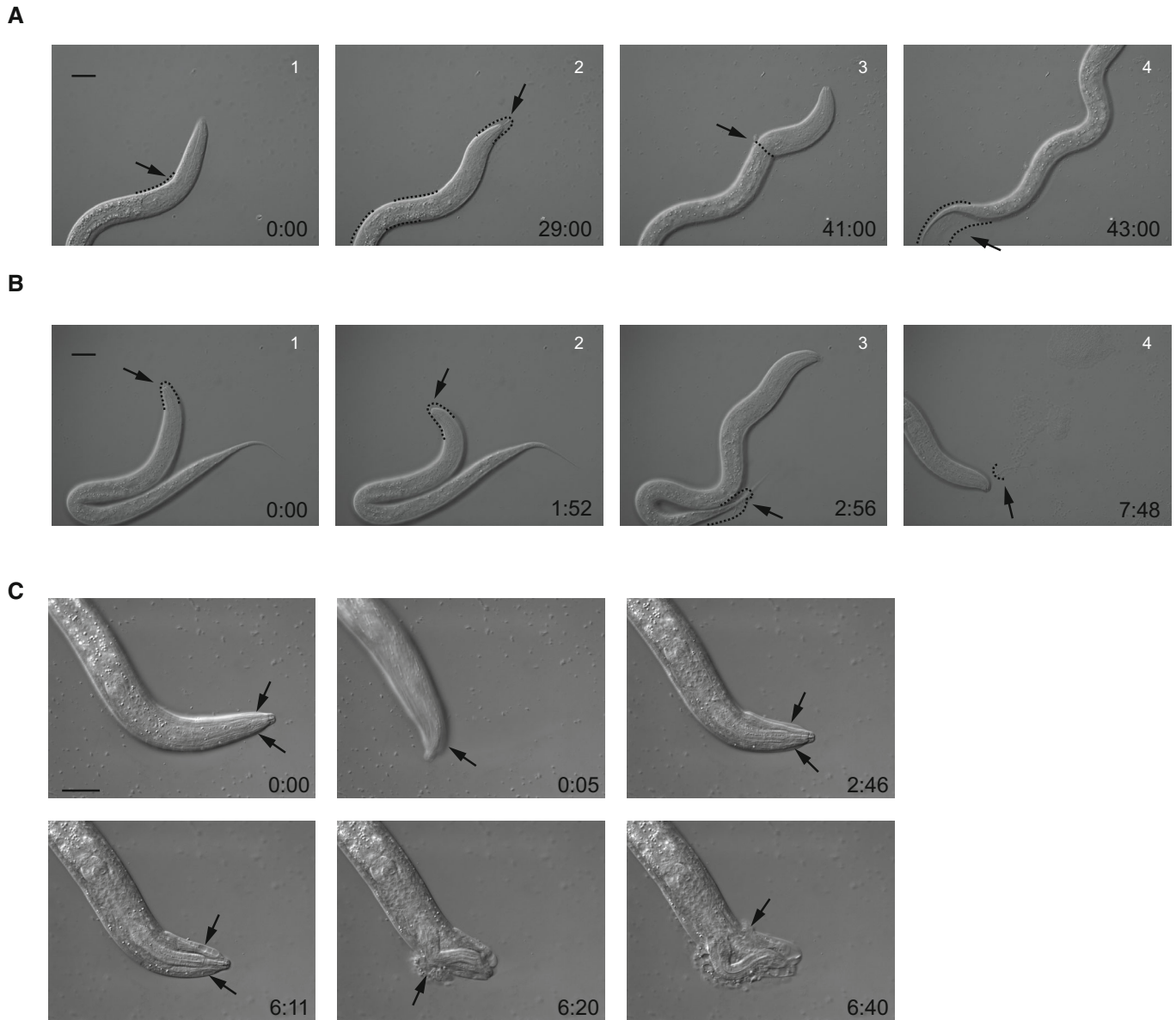
**Figure 3. GRH-1 is required for cuticular integrity and normal ecdysis.**

A, B Image sequence of N2 wild-type animals during M1. Lethargic animals were transferred to an agar pad and observed by DIC at 63× magnification and imaged every 20 s (A) or every 4 s (B), respectively. Selected images with time stamps are shown. Dashed lines indicate cuticle boundaries detached from the body. As reported previously (Singh & Sulston, 1978), two different sequences of events were observed: the pharyngeal lining is removed prior to ecdysis (A), or the pharyngeal lining is expelled after crawling out of the cuticle (B). Arrows indicate specific features of the molt. In (A): 1. Loosened cuticle, 2. Detachment of pharyngeal lining, 3. Crawling out of cuticle, 4. Final crawling out of cuticle. In (B): 1. Loosened cuticle, 2. Back-and-forth movements, 3. Crawling out of cuticle with pharyngeal lining still attached, 4. Pharyngeal lining expelled.

C Image sequence of an L1 synchronized *grh-1::aid* animal (HW2418) grown at 20°C on a 250 μM auxin-containing plate. A lethargic animal was transferred to an agar-pad on a microscopy slide and images were collected every 1 s, using DIC, 100× magnification. Time stamp (min:sec) is indicated. Arrows indicate phenotypic features: loosening of the cuticle (0:00); back-and-forth movements (0:05); inflation of the cuticle (2:46); vesicles underneath loosened cuticle (6:11); rupturing of the cuticle (6:20, 6:40).

Data information: Scale bars in A–C represent 20 μm. See also Movies EV1–EV3.

accumulation is also rhythmic. To test this, we examined a GRH-1::GFP::3xFLAG fusion protein expressed from the endogenous *grh-1* locus. We observed the first detectable signal in elongating embryos (Fig EV4A and B), that is, at the time when oscillatory gene expression initiates (Meeuse *et al*, 2020). In larvae, GFP signal accumulated in various cell types, including seam cells, vulva precursor cells, non-seam hypodermal cells, pharyngeal cells, and head neurons (Fig EV4C). Finally, in adults, which lack oscillatory gene expression (Meeuse *et al*, 2020), GFP levels were diminished or altogether absent in various tissues (Appendix Fig S5).
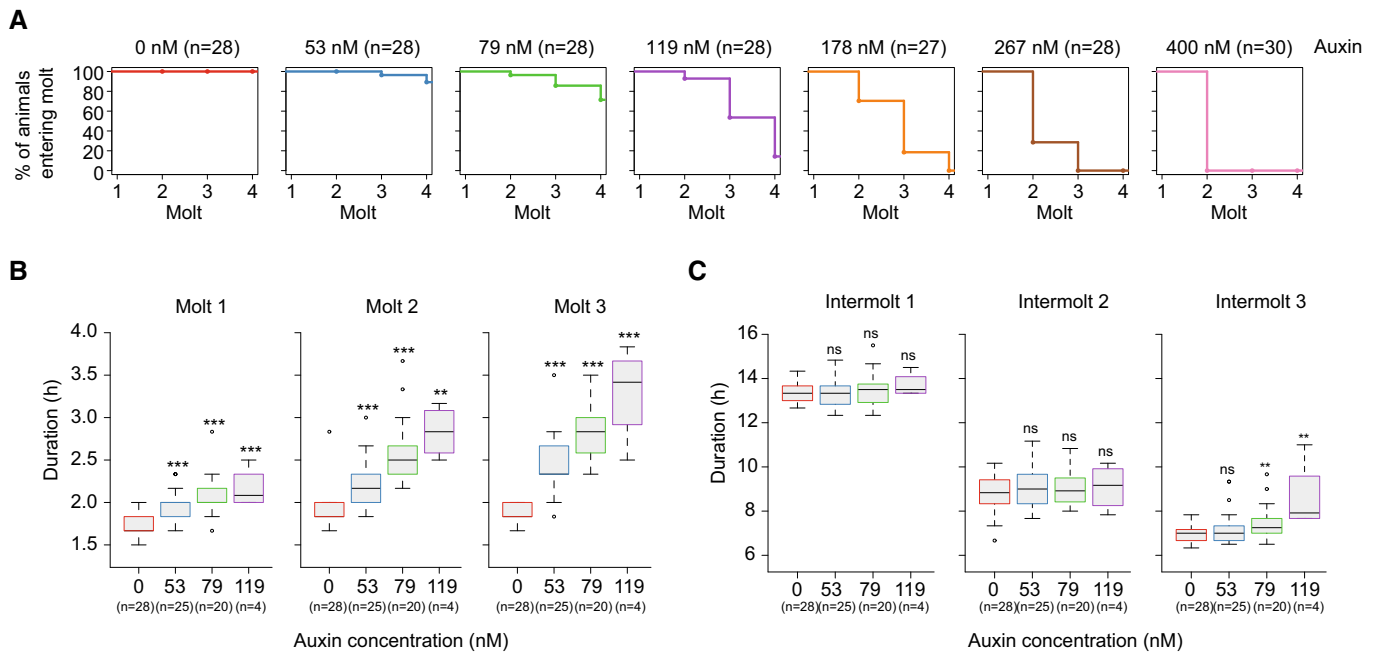
Figure 4. GRH-1 depletion extends molt duration in a dose-dependent manner.

A Quantification of the percentage of *grh-1::aid* animals constitutively expressing luciferase (HW2434) that enter each of four molts molt upon hatching into increasing concentrations of auxin as indicated. Appendix Fig S4 shows biological replication with a different set of concentrations.

B Boxplot showing the duration of M1, M2, and M3 of animals treated with indicated concentrations of auxin. Animals that failed to develop beyond M3 in (A) were excluded. The horizontal line represents the median, hinges extend to first and third quartiles, and the whiskers extend up to the most extreme value within 1.5*IQR (interquartile range) of the median. Significant differences relative to 0 nM auxin are indicated. *P*-values were determined by a non-parametric Wilcoxon rank sum test that does not assume normal distribution. ns: not significant, *$P < 0.05$, **$P < 0.01$, ***$P < 0.001$. Appendix Fig S4 shows biological replication with a different set of concentrations.

C Quantification of intermolt durations for the same animals as in (B).

Data information: See also Appendix Figs S3 and S4.

To study the dynamics of *grh-1* expression in more detail and relate it to progression through larval development, we performed time-lapse microscopy of single animals grown in micro-chambers, acquiring fluorescence and bright-field images in parallel and with high temporal resolution as described previously (Meeuse *et al*, 2020). We observed robust rhythmic GRH-1 accumulation with a peak before molt entry (Fig 6).

Molting requires oscillatory GRH-1 activity

The rhythmic accumulation of GRH-1 suggested that it could also exhibit rhythmic activity, such that it was required only during a certain window of each larval stage to support successful molting. To test this hypothesis, we initiated GRH-1 degradation at variable times in L2 by adding auxin and monitored developmental progression using the luciferase assay. Plotting luminescence traces sorted by the time when the animals entered molt 2 in a heatmap (Fig 7A and B) revealed a striking cutoff on the onset of the phenotype: addition of auxin up to 3 h before the M2 was sufficient for phenotypic onset at M2 exit (Fig 7B and C). However, if animals received auxin later than this, that is, within 3 h from M2 entry or during M2, they progressed through M2 and instead exhibited the phenotype at M3 exit (Fig 7B and C). We observed analogous outcomes when auxin was added in L3

(Appendix Fig S6). This period of auxin resistance is not explained by slow GRH-1 depletion kinetics, since auxin depletes GRH-1 effectively within <1 h (Fig 7D). Hence, a period exists in each larval stage during which GRH-1 is dispensable for molt completion. Although technical limitations have prevented us from testing whether constitutive expression of *grh-1* is compatible with development, the dynamic GRH-1 accumulation and a recurring need for GRH-1 for molting thus support a model of rhythmic GRH-1 activity during larval development.

GRH-1 binds to the promoters of oscillating genes enriched in a specific phase window

To identify potential targets of GRH-1, we performed ChIP-seq analysis using the endogenously tagged GRH-1::GFP::3xFLAG. This revealed 6,268 peaks of GRH-1 binding in the genome, of which 6,260 were assigned to 6,717 genes (Methods). Binding to these genes was highly reproducible in a biological replicate (Fig 8A). Moreover, motif enrichment analysis using HOMER (Heinz *et al*, 2010) revealed a binding motif similar to that of the orthologous human GRHL1/2 and *Drosophila* Grainyhead transcription factors (Fig 8B), validating our data and indicating functional conservation. Notably, 24.7% of all peaks overlapped a binding motif passing HOMER's default cutoff, and this fraction grew even further when
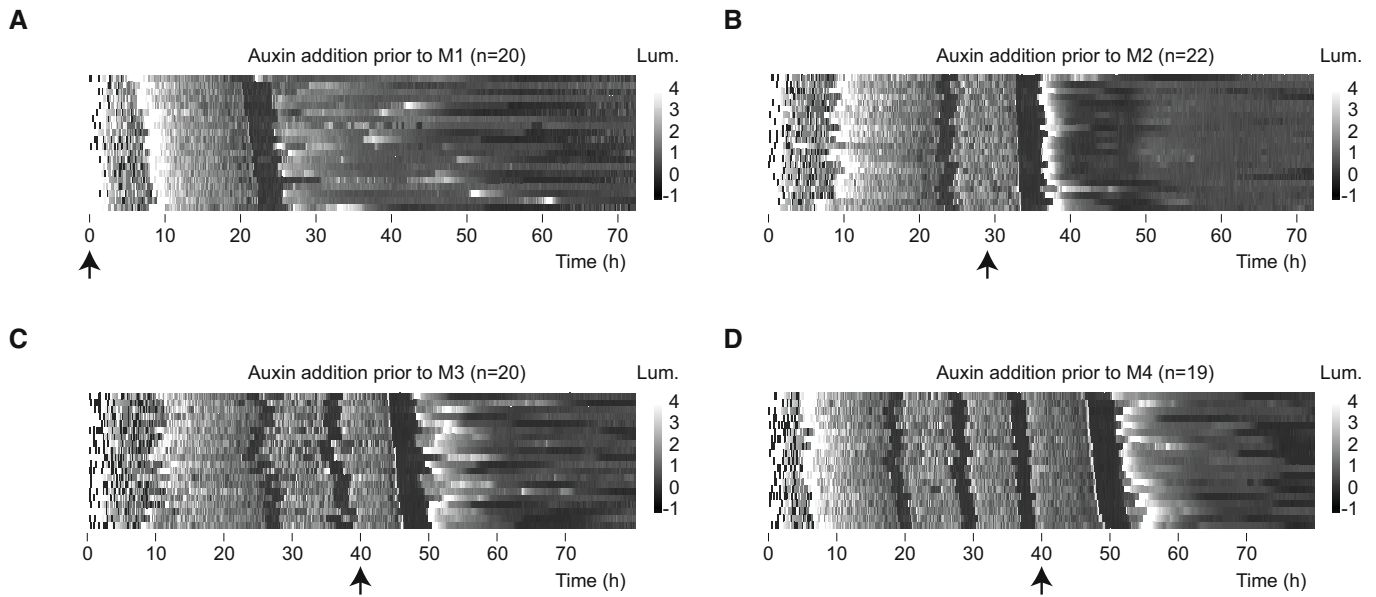
Figure 5. GRH-1 is required for successful completion of each molt.

A–D   Heatmaps showing trend-corrected luminescence (Lum, arbitrary units) of *grh-1::aid* animals constitutively expressing luciferase (HW2434). *T* = 0 h corresponds to time of plating embryos, which subsequently hatch at different times. Arrow indicates time point when 250 μM auxin was added, that is, prior to the first molt (A; M1), M2 (B), M3 (C), or M4 (D) larval stage. Note that for technical convenience in (A), auxin was provided at time of plating. Animals are sorted by entry into M1 (A), M2 (B), M3 (C), and M4 (D), respectively.

applying increasing fold enrichment thresholds to select peaks more stringently (Appendix Fig S7C).

We observed that putative direct targets (2,445 genes, operationally defined as those with assigned GRH-1 peaks of any enrichment that had a binding motif scoring above HOMER's threshold) were enriched for oscillating genes 2.3 fold ($P < 2.3e-60$, Fisher's exact test). Moreover, all the six screen hits, including *grh-1* itself, showed evidence of GRH-1 binding (Fig 8A), and *grh-1*, *nhr-23*, *nhr-25*, *blmp-1*, and *bed-3* all qualified as putative direct targets even up to a peak enrichment percentile of 95% ($\sim 3.59\times$). Hence, GRH-1 may function in a GRN with additional hits from our screen.

In the circadian clock, certain core clock factors also directly control a set of output genes, whose activity they regulate in a phase-specific manner (Patke *et al*, 2020). To test whether this was also true for GRH-1, we examined whether we could observe an enrichment of binding to the promoters of genes that are expressed in a specific phase, focusing on genes that have a "strong" GRH-1 peak (above the 80th percentile, i.e., $\sim 2.8\times$) and a "strong" motif match (i.e., above HOMER's threshold), to enrich for direct targets. When comparing the peak expression phases of GRH-1-bound genes to those of all other oscillating genes, we found that GRH-1 bound preferentially to genes with a peak phase between $\sim 270°$ and $\sim 70°$ (Figs 8C and EV5). This corresponds, at 25°C, to a ~ 3 h-window ending shortly after molt entry (Meeuse *et al*, 2020), agreeing well with the window of GRH-1 activity that we inferred from timed depletion (Fig 7) and the accumulation patterns of GRH-1 protein (Fig 6) and *grh-1* mRNA (preceding peak protein accumulation at a peak phase of at 269°, Meeuse *et al*, 2020). By contrast, GRH-1 binding was depleted for genes with a peak phase between $\sim 90°$ and 180° (Figs 8C and EV5). These findings lend further support to

rhythmic activity of GRH-1 and additionally suggest that GRH-1 may preferentially act as a transcriptional activator.

Discussion

Although molting is a fundamental feature of nematode development, little is known about the GRNs that control it. This is particularly true of the clock-type mechanisms thought to facilitate the regular occurrence of molts and synchronization of the various processes that they encompass. Here, we have demonstrated that rhythmic transcription drives oscillatory accumulation of a large fraction of genes. We devised a screen that identified six transcription factors important for molting and characterized the function of GRH-1. Our work provides a basis for elucidating the GRNs that support molting timing and execution through shaping or generating oscillatory gene expression.

Rhythmic transcription generates oscillating mRNA levels

Our previous work demonstrating rhythmic intronic RNA accumulation (Hendriks *et al*, 2014) implicated rhythmic transcription in the *C. elegans* larval oscillator. Time-resolved RNAPII ChIP-seq and reporter gene assays presented here now provide direct experimental support of this idea: globally, RNAPII ChIP-seq and mRNA-seq experiments yielded highly similar patterns, and several promoter fusion transgenes recapitulated the rhythmic accumulation of endogenous transcripts both qualitatively (as also noted in other instances Frand *et al*, 2005; Hao *et al*, 2006), and quantitatively at the level of phases and amplitudes.
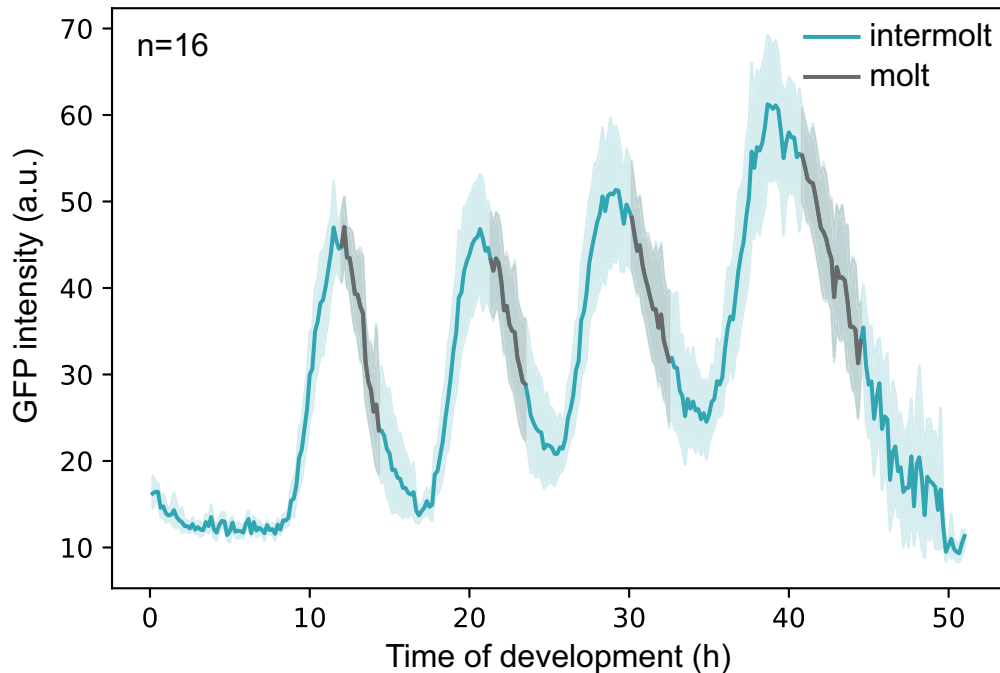
Figure 6. GRH-1 protein accumulates rhythmically before each molt.

Time-lapse imaging of *grh-1::gfp::3xflag* animals producing endogenously GFP-tagged GRH-1 protein. Average ± 95% confidence interval (cyan shading) is shown; gray color indicates average time of molts. See also Fig EV4, Appendix Fig S5.

Source data are available online for this figure.

Although our results demonstrate a major function of rhythmic RNA polymerase II recruitment in oscillating mRNA accumulation, we emphasize that, at least in specific cases, post-transcriptional regulatory mechanisms may serve to generate, shape, or damp oscillations, for example, through miRNA-mediated repression (Kim *et al*, 2013). The data we have presented here (Dataset EV1) may allow identification of such instances in the future, although we caution that the apparently lower dynamic range of RNAPII ChIP-seq poses a technical challenge.

**Identification of six transcription factors important for proper execution of molting cycles**

Prompted by the finding that oscillatory mRNA accumulation relies on rhythmic transcription, we decided to screen for transcription factors potentially involved in the process by identifying factors with knockdown-induced altered timing or reduced numbers of molts. In principle, the latter phenotype could also be caused by non-specific larval arrest or death, unrelated to functions in developmental timing or molts. It is thus a striking outcome of the screen, and a validation of our approach, that all six hits that we identified are indeed linked to molting, as shown here, in separate work (preprint: Hauser *et al*, 2021; Stojanovski *et al*, 2022), or evidenced by findings from the literature as discussed below. We propose that this reflects the pre-selection of our candidates as rhythmically expressed transcription factors.

Among the hits, we identified NHR-23/RORA/NR1F1, arguably the best-characterized molting transcription factor, whose depletion

was previously shown to cause a failure of ecdysis and larval arrest (Kostrouchova *et al*, 1998, 2001; Gissendanner *et al*, 2004; Frand *et al*, 2005; Kouns *et al*, 2011; preprint: Johnson *et al*, 2021; Patel *et al*, 2022) and which has a role in regulating the expression of collagens and hedgehog-related genes (Kouns *et al*, 2011).

The GRNs involving NHR-23's function in molting are not well understood. NHR-23 is orthologous to DHR3/NR1F1, an ecdysone-controlled fly transcription factor important for metamorphosis (Kostrouchova *et al*, 1998). In metamorphosis, DHR3 activates FTZ-F1 (Ou & King-Jones, 2013), the orthologue of another one of our screen hits, NHR-25/NR5A. Based on this orthology, and the finding that NHR-25 depletion impairs ecdysis (albeit more weakly and only in later molts than that of NHR-23), it was previously speculated that a regulatory interaction between the two proteins might be conserved in *C. elegans* and contribute to the molting process (Gissendanner & Sluder, 2000; Gissendanner *et al*, 2004). However, this notion has remained controversial (Kostrouchova *et al*, 2001), suggesting that further effort will be needed to understand whether and how NHR-25 – and NHR-23 – function in the molting cycle beyond their immediate regulation of cuticular components and their processing machinery.

Elsewhere, we have reported a detailed characterization of another screen hit, BLMP-1, which we find to be important for both molting timing and oscillatory gene expression (preprint: Hauser *et al*, 2021; Stojanovski *et al*, 2022), possibly through its function as a pioneer transcription factor (Stec *et al*, 2021). Consistent with our identification of BED-3 as a screen hit, BLMP-1 was previously reported to promote expression of *bed-3* and partially phenocopies
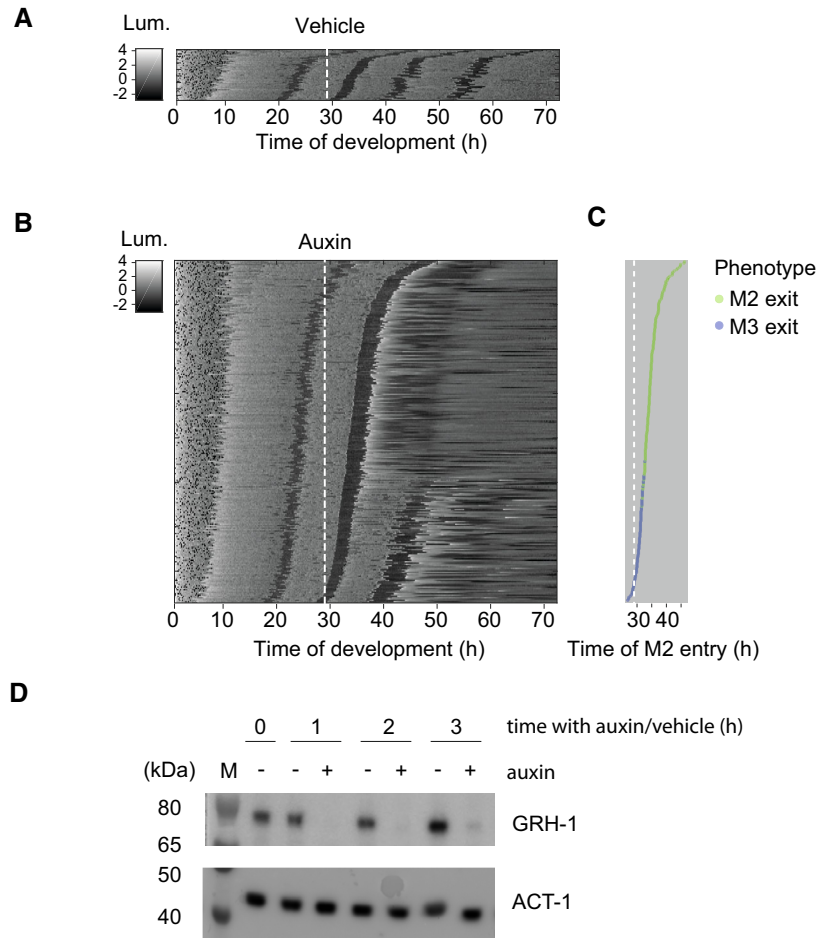
Figure 7. GRH-1 functions prior to the molt.

A, B   Heatmap showing trend-correct luminescence (Lum) of *grh-1::aid* animals (HW2434) treated with vehicle (0.25% ethanol) (A), or 250 µM auxin (B) at 29 h after plating (white dashed line). Black intensities reflect low luminescence during lethargus (molt). Embryos of various stages were plated to obtain an asynchronously hatching population. Luminescence traces are sorted by entry into molt 2 (M2) such that traces of early hatched animals are at the bottom and those of late hatched animals are at the top.

C   Plot of phenotype onset over time of auxin application relative to entry into molt 2 (M2 entry). Dots represent individual animals from (B) sorted by time of entry into M2 and colored according to whether the last observed molt in the luminescence trace was M2 (M2 exit phenotype; green) or M3 (M3 exit phenotype; blue). A white, dashed line indicates time of auxin application; dots to the left represent animals that entered M2 before auxin application, dots to the right represent animals that entered M2 after auxin application.

D   Western blot revealing rapid GRH-1 depletion in the *grh-1::aid* strain (HW2434) upon addition of 250 µM auxin. A synchronized culture of animals was grown in liquid at 20°C. After 21 h (denoted $t = 0$ h in the figure), the culture was split in two and either auxin or vehicle were added as indicated. Cultures were sampled hourly and protein lysates were probed by Western blotting using anti-FLAG and anti-actin antibodies as indicated.

Data information: See also Appendix Fig S6.
Source data are available online for this figure.

its mutant phenotypes (Yang *et al*, 2015). Finally, MYRF-1, also known as PQN-47, is required for ecdysis (Russel *et al*, 2011; Meng *et al*, 2017).

The Grainyhead transcription factor GRH-1 as a molting factor and candidate core clock gene

Here, we have focused on characterizing GRH-1. Previously the least studied factor among the six hits, it is a member of the Grainyhead/LSF1 protein family that controls epithelial cell fates across animals (Sundararajan *et al*, 2020). GRH-1 protein levels peak shortly before

molt entry, a time when GRH-1 activity is also required for a successful molt, and it preferentially binds the promoters of genes whose transcript levels peak before the molt. Hence, we propose that rhythmic GRH-1 accumulation helps to generate rhythmic GRH-1 activity that directs timely molting.

We show that the failure to complete development observed in the screen is due to a cuticle and ecdysis defect: the onset of ecdysis is delayed and the newly formed cuticle ruptures during ecdysis, particularly in the larval head region. Consistent with the view that generation of the new cuticle is defective, rupturing happens specifically after the onset of ecdysis, with tissue extrusion
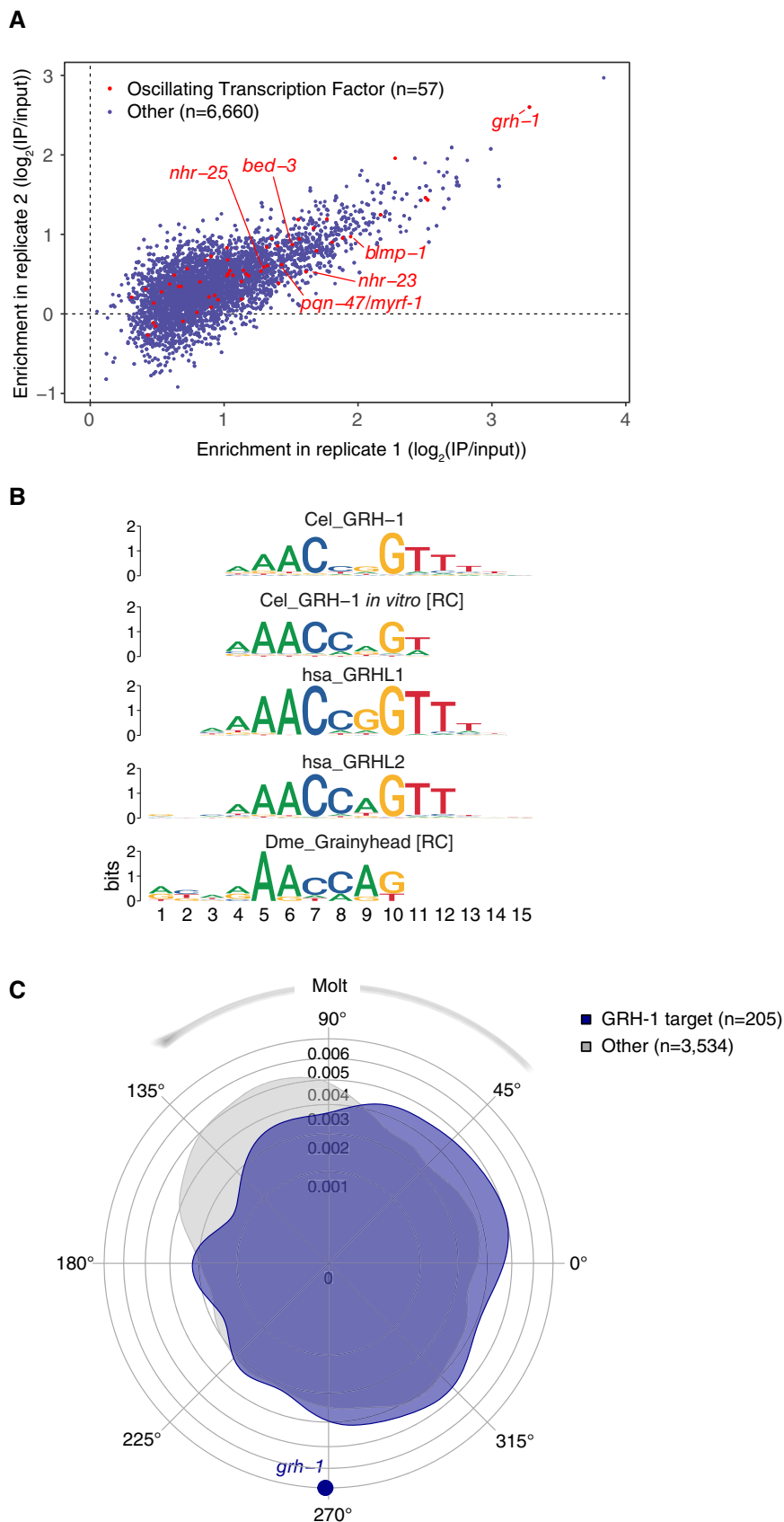
A

B

C

Figure 8.

Figure 8. GRH-1 binds to promoters of oscillating genes.

A   Scatter plot of GRH-1::GFP::3xFLAG ChIP-seq peak enrichments across two biological replicates, using an anti-GFP antibody to immunoprecipitate the endogenously tagged protein from L2 stage larval lysates. Peaks assigned to genes encoding rhythmically expressed transcription factors are plotted in red, all others in blue. Peaks assigned to candidate core clock genes identified in this study are labeled.

B   Consensus DNA binding motifs of Grainyhead family proteins. Cel_GRH-1 is the top scoring motif of length 12 observed in the GRH-1 ChIP-seq data. Cel_GRH-1 *in vitro* was re-built using binding site sequences provided in (Venkatesan *et al*, 2003); hsa_GRHL1 & 2 were extracted from JASPAR 2018 (https://jaspar2018.genereg. net), and Dme_Grainyhead was extracted from FlyFactorSurvey (https://mccb.umassmed.edu/ffs/). [RC] denotes motifs that have been automatically reverse-complemented for better alignment with other motifs.

C   Smoothed rose plot showing peak phase distributions of putative direct GRH-1 targets among oscillating genes. Genes are defined as GRH-1 targets if they contain a GRH-1 ChIP-seq peak with a fold enrichment over input at or exceeding 80% of all peaks that additionally overlaps a putative binding site scoring above the HOMER-derived threshold (Heinz *et al*, 2010) (Appendix Fig S7). Figure EV5 shows phase distributions for enrichment cut-offs of various stringencies. Approximate time of molt and the peak phase of *grh-1* mRNA accumulation are indicated by an arc and a dot, respectively.

occurring after the old (outer) cuticle has already visibly detached from the worm body. Indeed, the notion of impaired cuticle biogenesis is also consistent with cuticle defects in GRH-1-depleted *C. elegans* embryos, which do not undergo ecdysis (Venkatesan *et al*, 2003), although it remains possible that inappropriate proteolytic activities during ecdysis might additionally damage the newly formed cuticle. Finally, although lethality upon GRH-1 depletion was fully penetrant when animals were grown on plates, cuticle rupturing was not, suggesting that GRH-1 is more generally required for animal viability.

Soft, thin, and granular cuticles, prone to rupturing, are also a hallmark of *Drosophila* Grainyhead mutant animals (Nüsslein-Volhard *et al*, 1984; Bray & Kafatos, 1991). In mammals, *Grhl1* and *Grhl3* are dynamically expressed in the epidermis (Joost *et al*, 2016, 2020) and control epidermal differentiation (Yu *et al*, 2006), wound healing and eye lid closure (Boglev *et al*, 2011). Hence, our findings agree with a fundamental, evolutionarily conserved role of Grainyhead proteins in epidermis and ECM development and remodeling. It will thus be interesting to determine, in future work, the direct transcriptional outputs of GRH-1 and the GRNs that enable its dynamic expression. Our GRH-1 ChIP-seq analysis points to BED-3 and NHR-23 as particularly interesting candidates for future functional analysis.

Finally, we note that the orthologues of additional screen hits that we found function in development and regeneration of mammalian skin and its appendages, notably hair. We are particularly intrigued by the apparent parallels between *C. elegans* molting and the mammalian hair follicle cycle. This process of rhythmic homeostatic skin regeneration is controlled by a poorly characterized "hair follicle clock," modulated by circadian rhythms (Paus & Foitzik, 2004; Plikus *et al*, 2015). Mutations in the mouse orthologues of *blmp-1* and *nhr-23*, respectively, *Prdm1* and *Rora*, impair the proper execution of hair follicle cycles (Steinmayr *et al*, 1998; Magnusdottir *et al*, 2007; Telerman *et al*, 2017), while *grhl1* ablation causes hair coat defects related to hair anchoring and potentially other processes (Wilanowski *et al*, 2008).

In summary, we propose that this study identifies and characterizes several factors linked to a molting cycle oscillator that may have a functional correspondence in other animals, and that their further dissection provides a path to a molecular-mechanistic and systems understanding of gene expression oscillations in *C. elegans*. Additionally, we propose that *C. elegans* molting could serve as a powerful and genetically accessible model of animal skin development and regeneration.

Materials and Methods

C. elegans strains

The Bristol N2 isolate was used as the wild-type reference. We generated or used the additional strains listed below. A "PEST" degron sequence was included for the transcriptional reporters to destabilize the GFP protein and thereby enable detection of production dynamics (Meeuse *et al*, 2020).

rde-1(ne219) V (Tabara *et al*, 1999).

HW1360: *xeSi131[F58H1.2p::gfp::h2b::pest::unc-54 3′, unc-119+] II* (this study).

HW1361: *xeSi132[R12E2.7p::gfp::h2b::pest::unc-54 3′, unc-119+] II* (this study).

HW1370: *xeSi136[F11E6.3p::gfp-h2b-pest::unc-54 3′UTR; unc-119+] II* (Meeuse *et al*, 2020).

HW1371: *xeSi137[F33D4.6p:: gfp::h2b::pest::unc-54 3′UTR; unc-119+] II* (this study).

HW1372: *xeSi138[C05C10.3p:: gfp::h2b::pest::unc-54 3′UTR; unc-119+] II* (this study).

HW1431: *xeSi160[daf-6Δ4p::gfp::h2b::pest::unc-54 3′UTR; unc-119+] II* (this study).

HW1939: *xeSi296 [eft-3p::luc::gfp::unc-54 3′UTR, unc-119(+)] II* (Meeuse *et al*, 2020).

HW1949: *xeSi301 [eft-3p::luc::gfp::unc-54 3′UTR, unc-119(+)] III* (this study).

HW1984: *ieSi57 [eft-3p::TIR1::mRuby::unc-54 3′UTR, cb-unc-119 (+)] II; xeSi301 [eft-3p::luc::gfp::unc-54 3′UTR, unc-119(+)] III* (this study).

HW2079: *xeSi376 [eft-3p::TIR1::mRuby::unc-54 3′UTR, cb-unc-119(+)] III* (this study).

HW2150: *xeSi296 [eft-3p::luc::gfp::unc-54 3′UTR, unc-119(+)] II; rde-1(ne219) V* (this study).

CA1200: *ieSi57 [eft-3p::TIR1::mRuby::unc-54 3′UTR, cb-unc-119 (+)] II* (Zhang *et al*, 2015).

HW2418: *grh-1(xe135(grh-1::aid::3xflag)) I; xeSi376 [eft-3p:: TIR1::mRuby::unc-54 3′UTR, cb-unc-119(+)] III* (this study).

HW2434: *grh-1(xe135(grh-1::aid::3xflag)) I; xeSi296 [eft-3p::luc:: gfp::unc-54 3′UTR, unc-119(+)] II; EG8080, xeSi376 [eft-3p::TIR1:: mRuby::unc-54 3′UTR, cb-unc-119(+)] III* (this study).

HW2526: *xeSi440[dpy-9p::gfp::H2B::Pest::unc-54 3′UTR; unc-119+] II* (Meeuse *et al*, 2020).

HW2533: *xeSi442[col-10p::gfp::H2B::Pest::unc-54 3′UTR; unc-119+] II* (this study).

HW2603: *grh-1(syb616(grh-1::gfp::3xflag))* I (this study; custom-made by SunyBiotech).

IG274: *frIs7[nlp-29p::GFP + col-12p::DsRed] IV* (Pujol *et al*, 2008).

Generation of transgenic animals

Endogenous *aid::3xflag*-tagging *grh-1* and generation of *grh-1(0)* mutants by CRISPR/Cas9-mediated editing was performed using the previously published *dpy-10(cn64)* co-conversion protocol (Arribere *et al*, 2014). For the sgRNA plasmid, we inserted the sgRNA sequence (5′ agaggtttactctcatgagt 3′) into *Not*I-digested pIK198 (Katic *et al*, 2015) by Gibson assembly (Gibson *et al*, 2009).

For *aid::3xflag* tagging, we used hybridized MM116 (5′ AAT TGCAAATCTAAATGTTTagaggtttactctcatgagtGTTTAAGAGCTATGC TGGAA 3′) and MM117 (5′ TTCCAGCATAGCTCTTAAACactcatgag agtaaacctctAAACATTTAGATTTGCAATT 3′). An *aid::linker::3xflag*-linker cassette was synthesized as gBlocks® Gene Fragments (Integrated DNA Technologies) with 50 bp homology arms to the *grh-1* locus before the stop codon: 5′ CCACGTTAATCGAGGTGGCTCC CACCAATCCAAACTCGTATTCCAACTCAATGCCTAAAGATCCAGC CAAACCTCCGGCCAAGGCACAAGTTGTGGGATGGCCACCGGTGAG ATCATACCGGAAGAACGTGATGGTTTCCTGCCAAAAATCAAGCGG TGGCCCGGAGGCGGCGGCGTTCGTGAAGAGTACCTCAGGCGGCTC GGGTGGTACTGGCGGCAGCGACTACAAAGACCATGACGGTGATTA TAAAGATCATGACATCGATTACAAGGATGACGATGACAAGAGTAC TAGCGGTGGCAGTGGAGGTACCGGCGGAAGCTGAGAGTAAACCTC TTTAGGTTCTTGTCTTAATTCTCTTAAAGGAGGACT 3′. Wildtype animals were injected with 10 ng/µl gBlock, 100 ng/µl sgRNA plasmid, 20 ng/µl AF-ZF-827 (Arribere *et al*, 2014), 50 ng/µl pIK155 (Katic *et al*, 2015), and 100 ng/µl pIK208 (Katic *et al*, 2015). Genome editing was confirmed by sequencing.

HW2603: *grh-1(syb616(grh-1::gfp::3xflag))* was custom-generated by Suny Biotech and contains the following sequence inserted upstream of, and replacing, the endogenous TGA stop codon: AGTACTAGCGGTGGCAGTGGAGGTACCGGCGGAAGCAT GAGTAAAGGAGAAGAACTTTTCACTGGAGTTGTCCCAATTCTTGT TGAATTAGATGGTGATGTTAATGGGCACAAATTTTCTGTCAGTGG AGAGGGTGAGGGTGATGCAACATACGGAAAACTTACCCTTAAATT TATTTGCACTACTGGAAAACTACCTGTTCCATGGGTAAGTTTAAA CATATATATACTAACTAACCCTGATTATTTAAATTTTCAGCCAACA CTTGTCACTACTTTCTGTTATGGTGTTCAATGCTTCTCGAGATACC CAGATCATATGAAACAGCATGACTTTTTCAAGAGTGCCATGCCCG AAGGTTATGTACAGGAAAGAACTATATTTTTCAAAGATGACGGGA ACTACAAGACACGTAAGTTTAAACAGTTCGGTACTAACTAACCAT ACATATTTAAATTTTCAGGTGCTGAAGTCAAGTTTGAAGGTGATA CCCTTGTTAATAGAATCGAGTTAAAAGGTATTGATTTTAAAGAAG ATGGAAACATTCTTGGACACAAATTGGAATACAACTATAACTCAC ACAATGTATACATCATGGCGGACAAACAAAGAATGGAATCAAA GTTGTAAGTTTAAACATGATTTTACTAACTAACTAATCTGATTTA AATTTTCAGAACTTCAAAATTAGACACAACATTGAAGATGGAAGC GTTCAACTAGCAGACCATTATCAACAAAATACTCCAATTGGCGAT GGCCCTGTCCTTTTACCAGACAACCATTACCTGTCCACACAATCTG CCCTTTCGAAAGATCCCAACGAAAAGAGAGACCACATGGTCCTTC TTGAGTTTGTAACAGCTGCTGGGATTACACATGGCATGGATGAAC TATACAAAAGTACCTCAGGCGGCTCGGGTGGTACTGGCGGCAGCG ATTATAAAGACCACGATGGAGACTATAAAGATCATGACATTGACT ACAAGGATGACGACGACAAGTAG.

Transgenic reporter strain generation

GFP reporters were cloned by Gibson assembly (Gibson *et al*, 2009). Promoter sequences were amplified from genomic DNA using the primers listed below (overhangs indicated in bold) and inserted into *Nhe*I-digested pYPH0.14 as previously described (Meeuse *et al*, 2020). Transgenic animals were obtained by single copy-integration of the transgene into the ttTi5605 locus (MosSCI site) on chromosome II in EG6699 animals (lines HW1360, 1,361, 1,370, 1,371, 1,372, 1,431, 1,939, 2,150, 2,526, 2,533) or into the universal MosSCI ttTi5605 site on chromosome III in EG8080 animals (lines HW1949, 1984, 2079), using the published MosSCI protocol (Frøkjær-Jensen *et al*, 2012).

Vector name	Inserts	Primers	Primer sequence
pYPH3	F58H1.2 promoter	F58H1.2 promoter FW 1 + OH	GCGTGTCAATAATATCACTCat agatgtatactaatgaaggtaatagc
		F58H1.2 promoter RV1 + OH	GCTAAGTCTAGACATcattc ctgcgtagaagcg
pYPH4	R12E2.7 promoter	R12E2.7 promoter FW 1 + OH	GCGTGTCAATAATATCACTC aaatttttaaaatatctttatttgaaaatt
		R12E2.7 promoter RV1 + OH	GCTAAGTCTAGACATcatgat gattgagatgtgttgaaa
pYPH8	F33D4.6 promoter	F33D4.6 promoter FW + OH	GCGTGTCAATAATATCACTCtgtg aaacggaaaaaccatgc
		F33D4.6 promoter RV + OH	GCTAAGTCTAGACATctgaaacat acatttaattctaattagt
pYPH5	F11E6.3 promoter	F11E6.3 FW1 + Overhang	GCGTGTCAATAATATCACTC aggaaaacctcaaattttgttaacact
		PF11E6.3 RV + Overhang	GCTAAGTCTAGACATCATggttacct aaaaatataaagctct
pYPH61	col-10 promoter	col-10 promoter FW + OH	GGGCGTGTCAATAATATCACT Catcttctttttcattttcaatct
		col-10 promoter RV + OH	CCATGGCTAAGTCTAGACATgact gaaagccaggtac
pYPH38	daf-6 promoter (Δ4–1.5 kb)	Pdaf-6delta4 FW1 + OH	GCGTGTCAATAATATCACTC cgccaatggggatttgt
		Pdaf-6 RV0 + OH	GCTAAGTCTAGACATagaaaa cctgtaaaatacagaaac
pYPH9	C05C10.3 promoter	PC05C10.3 FW + Overhang	GCGTGTCAATAATATCACTC aagttatctttaaatcttgaataaaaa
		PC05C10.3 RV + Overhang	GCTAAGTCTAGACAT tttatctgaatgaaaattttttaattt

RNA polymerase II ChIP-seq

For RNAPII ChIP-seq, synchronized L1 wild-type larvae were grown at 25°C on plates seeded with concentrated OP50 bacteria. When seeking to infer dynamic patterns, dense sampling in a single time course yields superior results to sparse sampling with replicates

(Sefer *et al*, 2016). Hence, we performed a single, densely sampled time course in which we collected animals hourly from 22 h (90,000 worms) until 33 h (46,000 worms) developmental time. ChIP was performed as previously described (Miki *et al*, 2017). In short, worms were incubated in M9 with 2% formaldehyde for 30 min at room temperature with gentle agitation to allow protein-DNA crosslinking. Worms were lysed with beads using the FastPrep-24 5G machine (MP Biomedicals, settings: 8 m/s, 30 s on, 90 s off, 5 cycles). Lysates were sonicated using the Bioruptor Plus Sonication system (Diagenode, settings: 30 s on, 30 s off, 20 cycles). 250 μg sonicated chromatin was incubated with 10 μg mouse anti-RNA polymerase II CTD antibody (RRID:AB_306327, Abcam 8WG16) at 4°C for 2 h with gentle agitation, and subsequently with 45 μl Dynabeads Protein G (Thermo Fisher Scientific) at 4°C overnight with gentle agitation. Eluate was treated with 0.13 μg/μl RNase A and 1 μg/μl proteinase K. ChIP-seq libraries were prepared using NEBNext Ultra DNA Library Prep Kit for Illumina (New England Biolabs) and sequenced using the HiSeq 50 cycle single-end reads protocol on the HiSeq 2500 system.

Sequencing reads were aligned to the ce10 *C. elegans* genome using the qAlign() function (default parameters) from the QuasR package (Au *et al*, 2010; Gaidatzis *et al*, 2015) in R. Samples yielded 31 million to 42 million reads of which we could map 77–81%. ChIP-seq counts within 1-kb windows, that is, -500 bp to +500 bp around the annotated TSS (using Wormbase WS220/ce10 annotations), were scaled by total mapped library size per sample and $\log_2$-transformed after adding a pseudocount of 8. Genes with a mean scaled TSS window count of less than 8 across all samples were excluded. $\log_2$-transformed counts were then quantile-normalized using the normalize.quantiles() function from the preprocessCore library (Bolstad *et al*, 2003; Bolstad, 2021) in R. Finally, quantile-normalized values were row-centered for plotting in heatmaps.

RNA-sequencing for RNAPII ChIP-seq samples

For total RNA sequencing, aliquots of worms (~ 5,000 at late and ~ 10,000 at early time points) were collected from the same plates as for ChIP sequencing. RNA was extracted in Tri Reagent and DNase treated as described previously (Hendriks *et al*, 2014). Total RNA-seq libraries were prepared using Total RNA-seq ScriptSeq Library Prep Kit for Illumina (New England Biolabs) and sequenced using the HiSeq 50 cycle single-end reads protocol on the HiSeq 2500 system. RNA-seq data were mapped to the *C. elegans* genome (ce10) using the qAlign() function (splicedAlignment = TRUE, Rbowtie aligner version 1.16.0) from the QuasR package in R. Samples yielded between 41 million and 55 million reads of which we could map 72–81%, with the exception of timepoint 27 h, where only 54% of reads could be mapped. Exonic expression was quantified using the qCount() function from the R QuasR package and the exon annotation of the ce10 assembly (WormBase release WS220). Counts were scaled by total mapped library size for each sample. A pseudocount of 8 was added and counts were $\log_2$-transformed. Oscillating genes (Meeuse *et al*, 2020) were sorted by phase, and mean-centered expression was plotted in heatmaps.

GRH-1 ChIP sequencing and motif analysis

To confidently determine chromatin regions bound by GRH-1, we performed two ChIP-seq experiments using an anti-GFP antibody (RRID:AB_303395, Abcam ab290) to immunoprecipitate endogenously tagged GRH-1::GFP::3xFLAG from strain HW2603. Experiment one contained one "input" control sample and 3 IP "pulldown" samples using different salt concentrations (350 mM, 500 mM, 1 M) for protocol optimization and potential replication. We found 500 mM salt to work optimally and stayed with it for a validation experiment with independent biological samples, as well as a technical replicate made from a new aliquot of the chosen biological sample from experiment one.

The experiments used established sample preparation protocols ((Askjaer *et al*, 2014) & D. Thurtle-Schmidt, personal communication). Samples were prepared by synchronizing HW2603 larvae by hatching them in the absence of food followed by plating on NA22-containing and peptone-rich XL plates at 25°C. For each sample, 5 million animals were collected in phosphate-buffered saline, pH7.4 (PBS; 137 mM NaCl, 2.7 mM KCl, 10 mM Na_2HPO_4, and 1.8 mM KH_2PO_4) supplemented with protease inhibitors (1 mM PMSF +1 tablet cOmplete EDTA-free (Roche, Ref.: 11873580001) per 50 ml PBS) at 15 h and 19 h after plating, and "popcorn" was created by dripping resuspended larvae into liquid nitrogen. Popcorn from both time points was pooled and lysate prepared by grinding the popcorn, crosslinking with 1.1% formaldehyde, and sonication with a Diagnode Biorupter Pico. For the chromatin immuno-precipitation, 50 μl of protein G Dynabeads (10003D, ThermoFisher Scientific) were incubated with 5 μg of anti-GFP antibody (RRID:AB_303395, ab290, Abcam) for 4 h rotating at 4°C. One hundred micrograms of chromatin was added, and incubated over night at 4°C rotating. Beads were washed and the elute was treated with proteinase K and RNase A, and DNA was purified using Zymo ChIP Concentrator Kit. Sequencing libraries were prepared using the ChIP-seq NEB Ultra protocol (New England Biolabs) and sequenced using the Illumina 50-Cycle Single-End reads protocol on the HiSeq2500.

Reads were mapped to the *C. elegans* genome (ce10) using the R (v 4.2.0) function qAlign() (options splicedAlignment = TRUE, Rbowtie) from the QuasR package (v 1.36.0). For quality control, read pileup was manually examined in the IGV browser (Thorvaldsdottir *et al*, 2013), and counts were examined for evidence of biases (such as mappability or GC content) across 500-bp tiles; only a negligeable bias of higher read counts for higher %GC was observed.

For each input/IP sample pairing in each experiment, peaks were identified using the callpeak command from MACS2 (version 2.1.3.3) (Zhang *et al*, 2008), with thresholding option "-m 2 50," effective genome size option "-g ce," and otherwise default parameters. For each pairing, peaks overlapping flagged "overmapped" tiles (i.e., tiles with clearly higher input levels than expected, Appendix Fig S7A) were excluded from further analysis (typically affecting less than ~ 1% of peaks for each pairing). The remaining peaks were compared across sample pairs and experiments and found to be highly reproducible (Fig 8).

For motif analysis, we filtered peaks to the 90% most enriched for the selected sample pairings. Motifs were identified using HOMER (version 4.11) (Heinz *et al*, 2010) on these peaks, using segment size option "-size given," background segment count option "-N 170000," for motifs lengths "-len 8,10,12," autonormalization "-nlen 3," and parallelization options. Additionally, HOMER was provided with either the full ce10 genome, or a version where "unmappable" regions (given our sequencing protocol, defined as any position of the ce10 genome where a 50 bp SE read cannot map

uniquely, established using function getMappableRegions() from R package swissknife v 0.37, https://github.com/fmicompbio/swissknife) had been masked. Results from all configurations were manually compared using aligned "sequence logo" representations generated by R package universalmotif's (v 1.14.1) function view_-motifs() with option use.type = "ICM". Top-scoring hits were found to be highly similar, with a same top hit that aligned well with known motifs from orthologous genes (Fig 8B). Hence, the longest top hit motif from experiment 1 (present in 6.4% of background and 31% of foreground, corresponding to a ~ 4.8-fold enrichment, for a *P*-value of 1e-687) was used in further analyses.

Using this selected motif, putative binding sites were predicted on the non-mitochondrial mappable segments of the ce10 genome, using the wrapper function findMotifHits() from R package mona-Lisa (v 1.2.0) (Machlab *et al*, 2022), using a minimum score of 6, method "matchPWM," and parallelization options. To evaluate peak-site agreement, the fraction of peaks with a predicted binding site, and the fraction of predicted binding sites with a peak, were established for various percentile-based thresholds of both site score and peak enrichment (Appendix Fig S7B and C). Using the HOMER-based site score threshold and no peak enrichment threshold, these values were 24.7 and 22.0%, respectively.

Analysis of oscillatory genes among putative GRH-1 targets

Predicted binding sites were assigned to peaks based on non-null overlaps, and summarized to the peak level by recording the number of sites, number of "strong" sites (i.e., scoring above HOMER's score threshold), and maximum site score. Peaks, in turn, were assigned to genes in a multi-step process. First, each gene model was projected down into a single "gene body" covering the entire range of all possible isoforms (resulting in the TSS of this "gene body TSS" being the 5′ distal TSS of all annotated isoforms). Then, peaks were assigned to genes by non-null overlap with their promoter region (1,000 bp upstream of gene body TSS), non-null overlap with their bodies (up to 30 kb away from the TSS), or by lying upstream of the gene body TSS (up to 30 kb), in this order of priority for each gene. As such, one peak (containing 0 to many sites) can be assigned to multiple genes, one gene can have multiple peaks assigned to it, but one (peak; gene) pair can only occur once.

To investigate enrichments in certain phases, we split oscillating genes into "putative targets" or "other" ("non-targets") based on having an assigned peak with an enrichment above a certain enrichment threshold, and containing at least one site above HOMER's score threshold, and then varied the enrichment threshold. For each threshold value, we calculated and plotted the (circularized) density of target and non-target genes.

RT-qPCR reporters

Gravid adult worms were bleached to obtain eggs which were incubated in M9 buffer overnight (12 to 16 h) on a rotating wheel. Hatched worms were thus synchronized by arrest in L1 due to starvation. The synchronized L1 population was plated onto agar plates with food (*E. coli*, OP50) to initiate synchronous larval development. The concentration of worms per plate varied between 1,000 and 4,000 worms per plate, depending on stage, with a total of 2,000–8,000 worms sampled at each time point (fewer worms for the last

time points, when larvae are bigger). Worms were collected hourly between 22 and 37 h at 25°C (for *gfp* reporter data) after plating synchronized L1. Worms were washed off the plate(s) and washed three times in M9 buffer. After washing, 1 ml Tri Reagent (MRC) was added. Samples were frozen in liquid nitrogen and stored overnight at −80°C. Conventional RNA isolation using phenol chloroform extraction (adapted from Bethke *et al*, 2009) was used to extract RNA which was then diluted to the same concentration for each sample and used as input for the Promega Protocol: "ImProm-II™ Reverse Transcription System" to convert RNA to cDNA. The resulting cDNA was diluted 1:1,000 to quantify actin transcript levels and 1:20 for endogenous transcripts. qPCR was then performed on a Step one Realtime PCR machine using primer pairs (of which one was exon-exon spanning to detect mature mRNA levels) specific to the reporters and the *gfp* transcript.

RT-qPCR primers

Transcript	Primer name	Description	Sequence
gfp	YPH120	RV exon-exon spanning primer	ACAAGTGTTGGCCATGGA
	YPH121	FW primer	CTTGTTGAATTAGATGGTGATGTT
F58H1.2	YPH126	FW primer	TGATGTCGTCCATGGGAT
	YPH127	RV exon-exon spanning primer	CCATACGTATCCATTCCCA
R12E2.7	YPH128	FW primer	TCTTCTCTGCTTCTGCTT
	YPH129	RV exon-exon spanning primer	CTCCTCCGCATGGGT
F11E6.3	YPH164	FW exon-exon spanning primer	CCCATCCGATGAAACGTCA
	YPH165	RV primer	TGGGGCGGTTTCTTCTTGA
F33D4.6	YPH166	FW exon-exon spanning primer	CCCTCCAATGATCAACTTG
	YPH167	RV primer	ATGAATCTTTCGTCTTGGAAGG
C05C10.3	YPH168	FW exon-exon spanning primer	TTAGTTGGCGGCTTCGGA
	YPH169	RV primer	GTCGAGTTTGAAGGAGCAAG
daf-6	YPH170	FW exon-exon spanning primer	CTATCACGAGGCCTTTCCA
	YPH171	RV primer	CCCCACAACGTCATATAACCAAA
col-10	YPH430	FW exon-exon spanning primer	GGTTCACGATGAGGTTCT
	YPH431	RV primer	GTTGAATGGGTTGACACG
dpy-9	YPH544	FW exon-exon spanning primer	GTAGAGTTGTGTAAGACCGAG
	YPH545	RV primer	GAGTACAAGCACAGCAGG
act-1	*act-1* FW qPCR	FW primer	GTTGCCCAGAGGCTATGTTC
	act-1 RV qPCR	RV primer	CAAGAGCGGTGATTTCCTTC

RT-qPCR analysis

From two technical replicates, the mean actin Ct values were subtracted from the mean target Ct values, to obtain a relative quantification, represented by delta Ct (dCt). To obtain the mean-normalized mRNA levels, the dCt mean of the time series was subtracted from each time point value first and then multiplied by −1. These values were then plotted to compare endogenous versus *gfp* mRNA levels.

Luciferase assays

Luciferase assays were performed as described before (Meeuse *et al*, 2020). In short, single embryos, expressing luciferase from a constitutive and ubiquitous promoter (transgene *xeSi296*) were placed in a 384-well plate (Berthold Technologies, 32505) by pipetting, and left to develop until adulthood in 90 μl S-Basal medium containing *E. coli* OP50 (OD_{600} = 0.9) and 100 μM Firefly D-Luciferin (p.j.k., #102111). Luminescence was measured using a luminometer (Berthold Technologies, Centro XS3 LB 960) every 10 min for 0.5 s for 72 h in a temperature-controlled incubator set to 20 degrees.

For auxin experiments, a 400× stock solution of 3-indoleacetic acid (auxin, Sigma Aldrich, I2886) in 100% ethanol was prepared. The stock solution was diluted 400-fold in the culture medium at the start of each experiment or at specific time points and in concentrations as indicated.

Luminescence data were analyzed using an automated algorithm (MATLAB code available on Github at: https://github.com/fmi-basel/ggrosshans_LuciferaseAssayAnalyzer) to detect the hatch and the molts with manual curation as appropriate, as described before (Meeuse *et al*, 2020). Completion of molts was scored by the presence of a drop in luminescence, followed by a period of stable and low luminescence and subsequent rise in luminescence. No statistical estimate of minimal sample size was performed prior to the experiment. Molt annotation occurred semi-automatically as described above; no additional efforts were made at blinding samples.

RNAi screen

To knock-down 92 "oscillating" transcription factors, we used the RNAi feeding method. *E. coli* HT115 bacteria carrying RNAi plasmids were obtained from either of the two genome-wide libraries, Ahringer library (Fraser *et al*, 2000; Kamath *et al*, 2003) or Vidal library (Rual *et al*, 2004), or cloned if unavailable (see generation of RNAi vectors).

Luciferase assays were performed as described above with the following adaptations: RNAi bacteria were grown in 5 ml auto-induction medium (2 mM $MgSO_4$, 3.3 g/l $(NH_4)2SO_4$, 6.8 g/l KH_2PO_4, 7.1 g/l Na_2HPO_4, 5 g/l glycerol, 0.5 g/l glucose, 2 g/l α-lactose, 100 μg/ml Amp in ZY medium (10 g/l tryptone, 5 g/l yeast extract)) at 37°C. Bacteria were diluted in S-Basal medium (OD600 = 0.45), with 100 μM Firefly D-luciferin (p.j.k., 102111) and 100 μg/ml Ampicillin.

We used HW1939 animals that express the *xeSi296* transgene. As a control strain, we used HW2150 animals expressing *xeSi296* in an *rde-1(ne219)* (Tabara *et al*, 1999) background, which are RNAi deficient. For each RNAi condition, we used two adjacent columns in the 384-wells plate, that is, 32 wells with 90 μl culture medium each. To avoid plate effects, the first eight wells of the first column and the last eight wells of the second column of the same RNAi condition were each filled with an HW1939 animal and the remaining wells each with an HW2150 animal.

To identify mutants, we inspected the heatmaps with trend-corrected luminescence (Olmedo *et al*, 2015) for aberrant duration or number of molts and intermolts.

Generation of RNAi vectors

For clones that were not available in the Ahringer or Vidal libraries, cDNA or genomic DNA was PCR amplified using the following primers:

Locus	Vector transformed	Insert	Primer	Primer sequence
nhr-5	pMM012_R	Y73F8A.21a cDNA	MM070 MM071	ccaccggttccatggct agcTTCTGGCGGTA ACAGTTCAA ttgatatcgaattcctg cagGATGTGAGTAT GGAATATTCGG
dmd-8	pMM013_R	T22H9.4 cDNA	MM076 MM077	ccaccggttccatggct agcCCCTGTCATCT TCTTCAAATGC ttgatatcgaattcctg cagGTTTCAGCGCA GCTAATTGC
bcl-11	pMM014_R	F13H6.1a cDNA	MM078 MM079	ccaccggttccatggc tagcAATAGAAACG TCTTCGGCGG ttgatatcgaattcctg cagTTAACGGTTGG TGTGACTGC
fkh-9	pMM015_R	K03C7.2b cDNA	MM080 MM081	ccaccggttccatggct agcGATTTGCTACG ATCACCCAT ttgatatcgaattcctg cagGGCCTTGATTG GAGAAAGTG
ztf-16	pMM016_R	R08E3.4a cDNA	MM082 MM083	ccaccggttccatggct agcCGACTACTGTA TTTTCCGAGTT ttgatatcgaattcctg cagCAGTTAACGAA AGTGATGACTC
sem-2	pMM017_R	C32E12.5.1 cDNA	MM084 MM085	ccaccggttccatggct agcGATCTCCAAAA ACCGCCCAA ttgatatcgaattcctg cagTGCATCGCTCC ATGGATAAT
grh-1	pMM018_R	Y48G8AR.1a cDNA	MM086 MM087	ccaccggttccatggc tagcGAAGAAGTCC GACGGTGAAT ttgatatcgaattcctg cagGAGTTTGGATT GGTGGGAGC
dmd-9	pMM019_R	Y67D8A.3 genomic DNA	MM088 MM089	ccaccggttccatggct agcCTTTGTTCCAG TTCAAACCAC

Locus	Vector transformed	Insert	Primer	Primer sequence
				ttgatatcgaattcctg cagAGAGGGAAGG AACTGATAGAC
tbx-7	pMM020_R	ZK328.8.1 genomic DNA	MM090 MM091	ccaccggttccatggct agcCCTCATGACAG ACAACTACT ttgatatcgaattcctg cagCAACAACTCCA AATCCACTT
M03D4.4b	pMM021_R	M03D4.4b cDNA	MM092 MM093	ccaccggttccatggc tagcTCGGACACAG ATTCATCACAAC ttgatatcgaattcctg cagTCCGGTGTTGC TGTATTTGTC
C08G9.2	pMM022_R	C08G9.2 cDNA	MM094 MM095	ccaccggttccatggc tagcTACCGGCAAG TGTACCAAAT ttgatatcgaattcctg cagACCTTCACATG GATCTACACAA
nhr-112	pMM023_R	Y70C5C.6a cDNA	MM096 MM097	ccaccggttccatggc tagcTTTTCCGCAG ATTCTATCACTC ttgatatcgaattcctg cagTATGATTCATC TCGCACACCA
ets-4	pMM024_R	F22A3.1a cDNA	MM098 MM099	ccaccggttccatggct agcATGCAATCTTC CAATCCAACC ttgatatcgaattcctg cagAGGCAGGAATT TGTACACCA
ztf-14	pMM025_R	M163.2 genomic DNA	MM102 MM103	ccaccggttccatggct agcGCCGTCCCTG CATAACTACTC ttgatatcgaattcctg cagAGAGAAGTGAG TTGCGGGAG
ztf-29	pMM026_R	Y66D12A.12 cDNA	MM104 MM105	ccaccggttccatggct agcCGTCACCGGC TCAACTTCCA ttgatatcgaattcctg cagCATGTTCTCCT CCTTTCGCTCT

PCR fragments were cloned into the RNAi feeding *Pml*I and *Sma*I digested L4440 vector (L4440 was a gift from Andrew Fire (Addgene plasmid # 1654; http://n2t.net/addgene:1654; RRID:Addgene_1654)) using Gibson assembly (Gibson *et al*, 2009) and transformed into *E. coli* HT115 bacteria.

Phenotype imaging

To image molting phenotypes, HW2418 worms were mounted on a 2% (w/v) agarose pad with a drop of M9 buffer (42 mM Na_2HPO_4, 22 mM KH_2PO_4, 86 mM NaCl, 1 mM $MgSO_4$). *grh-1::aid* animals were imaged on an Axio Imager Z1 (Zeiss) microscope. We acquired Differential Interference Contrast (DIC) images using a 100×/1.4 oil immersion objective and a TL Halogen Lamp (3.00 Volt, 900 ms

exposure). Images (1,388 × 1,040 pixels, 142.1 μm × 106.48 μm pixel size, 12 bit) were acquired every second from the moment that the cuticle became loose around the tip of the head until after the worm burst through the head, which took roughly 5 to 10 min. N2 animals were imaged on an Axio Imager Z2 (Zeiss) microscope. We acquired Differential Interference Contrast (DIC) images using a 63×/ 1.4 oil immersion objective and a TL Vis-LED Lamp (5.74 Volt, 17 ms (Fig 3A) or 19 ms (Fig 3B) exposure). Images (1,388 × 1,040 pixels, 225.56 μm × 169.01 μm pixel size, 12 Bit) were acquired at 20 s (Fig 3A) or 4 s (Fig 3B) intervals from the moment that the cuticle became loose around the tip of the head until the cuticle was shed.

Confocal imaging

To investigate the expression of endogenously tagged *grh-1*, mixed-stage HW2603 (*grh-1(syb616(grh-1::gfp::3xflag))I*) worms were grown at 25°C. For confocal microscopy, worms of different stages (eggs, larvae, and adults) were mounted on a 2% (w/v) agarose pad in a drop of 10 mM levamisole (Fluca Analytical, 31742) for immobilization. Worms were imaged on Axio Imager M2 (upright microscope) + Yokogawa CSU W1 Dual camera T2 spinning disk confocal scanning unit driven by Visiview 3.1.0.3. DIC and fluorescent images were acquired with a 40×/1.3 oil immersion objective (2048 × 2048 pixels, 16-bits) with 10 ms and 150 ms of exposure time, respectively. Images were processed using ImageJ (Fiji) software with identical settings to compare different stages of worm.

Time-lapse single-worm imaging

To investigate the temporal expression pattern of endogenously tagged *grh-1*, single animals of the strain HW2603 (*grh-1(syb616(grh-1::gfp::3xflag))I*) were observed by time lapse imaging as previously described (Meeuse *et al*, 2020) with slight modifications. Briefly, an array of microchambers (Bringmann, 2011; Turek *et al*, 2015) was made of 4.5% agarose in S-Basal medium (Stiernagle, 2005). OP50 bacteria were grown on agar plates, scraped off, and transferred to the chambers. Single eggs were placed on the chambers and flipped into a glass coverslip surrounded by a silicone insulator. Low melting agarose (3.5%) was used to seal the edges of the array, which was subsequently mounted on a glass slide for imaging. We imaged animals using a 2× sCMOS camera model (T2) on an Axio Imager M2 (upright microsocope) CSU_W1 Yokogawa spinning disk microscope with a 20× air objective (NA = 0.8). The 488 nm laser was set to 70% power, with 10 ms exposure and a binning of 2. Brightfield and fluorescent images were taken in parallel using a motorized z-drive with a 2-μm step size and 23 images per z-stack for a total duration of 60 h at 10 min time intervals in a ~ 21°C room.

Single-worm imaging data analysis

Brightfield images were segmented using a Convolutional Neural Network (CNN v2). The segmentation method takes as an input a 3D image stack with one well in its field of view. It first performs a min-projection along the Z-axis, resamples the resulting 2D image to a fixed input size, subtracts background, and rescales the [min, max] intensity range to [−1, 1]. This preprocessing renders the pipeline more robust to certain types of variabilities across acquisitions from different microscopes. The preprocessed input is then

transformed by a UNet-like CNN (Ronneberger *et al*, 2015) with four levels and an input size of 320×320. It outputs a 2D probability map indicating whether a particular location is considered part of the worm (i.e., foreground) or not. The resulting probability map is resampled back to the original input's pixel spacing to re-establish the 1:1 pixel correspondence. At inference, the CNN is applied on all four 90-degree rotated versions of the preprocessed input image, and the four outputs rotated back and averaged before resampling. For saving the probability maps, their range is rescaled from [0, 1] to [0, 255] and discretized to 8-bit.

The CNN is trained on min-projected stacks where the foreground was manually annotated using ITKSnap (Yushkevich *et al*, 2006). The dataset consists of 1,104 image-annotation pairs from different acquisitions, split into 948 for training, 105 for validation, and 51 for testing. For online training data augmentation, we rely on additive Gaussian noise, random flips, and 90° rotations. A weighted binary cross-entropy loss is optimized using Adam (Kingma & Ba, 2015) during training. Using a default threshold of 127 on the segmentation probability, GFP intensities were quantified on the segmented images using a previously published KNIME workflow (Meeuse *et al*, 2020). In short, worms are straightened and the GFP intensity of the worm is max projected to one pixel line for each time point. Background-subtracted mean GFP intensities are determined from 20 to 80% of the anterior–posterior axis for each time point. To annotate molts, each image was visually inspected for molt entry and molt exit by scrolling through z-stack of the individual timepoints. The GFP intensities and lethargus data were plotted together in Python v3.9 using the Seaborn package.

Western blot

To examine the kinetics of GRH-1-AID-3xFLAG depletion by auxin, synchronized *grh-1(xe135); eft-3p::luc; eft-3p::TIR1* L1-stage animals (HW2434) were cultured in liquid (S-Basal supplemented with OP50, $OD_{600} = 3$, 1,000 animals/ml) at 20°C. After 21 h, when animals had reached early L2 stage, the culture was sampled, split in two, and supplemented with 250 μM auxin or an equivalent amount of vehicle, respectively, followed by hourly sampling. At each time point, 10,000 animals were collected and washed three times with M9 buffer (42 mM Na_2HPO_4, 22 mM KH_2PO_4, 86 mM NaCl, 1 mM $MgSO_4$). Lysates were made by disruption (FastPrep-24, MP Biomedicals, 5 cycles, 25 s on, 90 s off), sonication (Biorupter, Diagnode, 10 cycles, 30 s on, 60 s off) and subsequent boiling. Proteins were separated by SDS-PAGE and transferred to a PVDF membrane by semi-dry blotting. Antibodies were used at the following dilutions: mouse anti-FLAG-HRP (1:1,000, RRID:AB_439702, Sigma Aldrich Cat #A8592), mouse anti-Actin, clone C4 (1:5,000, RRID: AB_2223041, Millipore MAB1501), mouse IgG HRP linked (1:7,500, NXA931V, GE Healthcare). We used ECL Western Blotting detection reagent (RPN2232 and RPN2209, GE Healthcare) and ImageQuant LAS 4000 chemiluminescence imager (GE Healthcare) for detection.

Data availability

All sequencing data generated for this study have been deposited in NCBI's Gene Expression Omnibus (Edgar *et al*, 2002) and are accessible through GEO SuperSeries accession number GSE169642

(RNAPII ChIP-sequencing and RNA-sequencing) and SuperSeries accession number GSE213510 (GRH-1 ChIP-sequencing replicates), respectively. The code for the main bioinformatic analyses for the RNAPII timecourse ChIP-seq, timecourse mRNA-seq, GRH-1 ChIP-seq, and imaging CNN is provided *as is* in a Github repository for this paper: https://github.com/fmi-basel/ggrosshans_grh-1_paper. Published research reagents from the FMI are shared with the academic community under a Material Transfer Agreement (MTA) having terms and conditions corresponding to those of the UBMTA (Uniform Biological Material Transfer Agreement).

Expanded View for this article is available online.

Author contributions

Milou W M Meeuse: Conceptualization; formal analysis; funding acquisition; investigation; writing – original draft. **Yannick P Hauser:** Formal analysis; investigation; writing – review and editing. **Smita Nahar:** Formal analysis; funding acquisition; investigation; writing – review and editing. **A Alexander T Smith:** Formal analysis; investigation; writing – review and editing. **Kathrin Braun:** Investigation; writing – review and editing. **Chiara Azzi:** Investigation; writing – review and editing. **Markus Rempfler:** Methodology. **Helge Großhans:** Conceptualization; supervision; funding acquisition; writing – original draft; project administration.

Disclosure and competing interests statement

The authors declare that they have no conflict of interest.

References

Arribere JA, Bell RT, Fu BX, Artiles KL, Hartman PS, Fire AZ (2014) Efficient marker-free recovery of custom genetic modifications with CRISPR/Cas9 in *Caenorhabditis elegans*. *Genetics* 198: 837–846

Askjaer P, Ercan S, Meister P (2014) Modern techniques for the analysis of chromatin and nuclear organization in *C. elegans*. *WormBook* 1–35

Au KF, Jiang H, Lin L, Xing Y, Wong WH (2010) Detection of splice junctions from paired-end RNA-seq data by SpliceMap. *Nucleic Acids Res* 38: 4570–4578

Bethke A, Fielenbach N, Wang Z, Mangelsdorf DJ, Antebi A (2009) Nuclear hormone receptor regulation of microRNAs controls developmental progression. *Science* 324: 95–98

Boglev Y, Wilanowski T, Caddy J, Parekh V, Auden A, Darido C, Hislop NR, Cangkrama M, Ting SB, Jane SM (2011) The unique and cooperative roles of the grainy head-like transcription factors in epidermal development reflect unexpected target gene specificity. *Dev Biol* 349: 512–522

Bolstad BM (2021) *preprocessCore: a collection of pre-processing functions*. R package version 1.56.0

Bolstad BM, Irizarry RA, Astrand M, Speed TP (2003) A comparison of normalization methods for high density oligonucleotide array data based on variance and bias. *Bioinformatics* 19: 185–193

Brancati G, Großhans H (2018) An interplay of miRNA abundance and target site architecture determines miRNA activity and specificity. *Nucleic Acids Res* 46: 3259–3269

Bray SJ, Kafatos FC (1991) Developmental function of Elf-1: an essential transcription factor during embryogenesis in drosophila. *Genes Dev* 5: 1672–1683

Bringmann H (2011) Agarose hydrogel microcompartments for imaging sleep- and wake-like behavior and nervous system development in *Caenorhabditis elegans* larvae. *J Neurosci Methods* 201: 78–88

Cohen JD, Sundaram MV (2020) *C. elegans* apical extracellular matrices shape epithelia. *J Dev Biol* 8: 23

Cohen JD, Sparacio AP, Belfi AC, Forman-Rubinsky R, Hall DH, Maul-Newby H, Frand AR, Sundaram MV (2020) A multi-layered and dynamic apical extracellular matrix shapes the vulva lumen in *Caenorhabditis elegans*. *Elife* 9: e57874

Edgar R, Domrachev M, Lash AE (2002) Gene expression omnibus: NCBI gene expression and hybridization array data repository. *Nucleic Acids Res* 30: 207–210

Frand AR, Russel S, Ruvkun G (2005) Functional genomic analysis of *C. elegans* molting. *PLoS Biol* 3: e312

Fraser AG, Kamath RS, Zipperlen P, Martinez-Campos M, Sohrmann M, Ahringer J (2000) Functional genomic analysis of *C. elegans* chromosome I by systematic RNA interference. *Nature* 408: 325–330

Frøkjær-Jensen C, Davis MW, Ailion M, Jorgensen EM (2012) Improved Mos1-mediated transgenesis in *C. elegans*. *Nat Methods* 9: 117–118

Gaidatzis D, Lerch A, Hahne F, Stadler MB (2015) QuasR: quantification and annotation of short reads in R. *Bioinformatics* 31: 1130–1132

Gibson DG, Young L, Chuang R-Y, Venter JC, Hutchison CA, Smith HO (2009) Enzymatic assembly of DNA molecules up to several hundred kilobases. *Nat Methods* 6: 343–345

Gissendanner CR, Sluder AE (2000) Nhr-25, the *Caenorhabditis elegans* ortholog of ftz-f1, is required for epidermal and somatic gonad development. *Dev Biol* 221: 259–272

Gissendanner CR, Crossgrove K, Kraus KA, Maina CV, Sluder AE (2004) Expression and function of conserved nuclear receptor genes in *Caenorhabditis elegans*. *Dev Biol* 266: 399–416

Hao L, Johnsen R, Lauter G, Baillie D, Burglin TR (2006) Comprehensive analysis of gene expression patterns of hedgehog-related genes. *BMC Genomics* 7: 280

Hauser YP, Meeuse MWM, Gaidatzis D, Großhans H (2021) The BLMP-1 transcription factor promotes oscillatory gene expression to achieve timely molting. *bioRxiv* https://doi.org/10.1101/2021.07.05.450828 [PREPRINT]

Heinz S, Benner C, Spann N, Bertolino E, Lin YC, Laslo P, Cheng JX, Murre C, Singh H, Glass CK (2010) Simple combinations of lineage-determining transcription factors prime cis-regulatory elements required for macrophage and B cell identities. *Mol Cell* 38: 576–589

Hendriks G-J, Gaidatzis D, Aeschimann F, Großhans H (2014) Extensive oscillatory gene expression during *C. elegans* larval development. *Mol Cell* 53: 380–392

Johnson LC, Aguilera J, Levenson MT, Rechtsteiner A, Vo AA, Ragle JM, Ward JD (2021) Conditional depletion reveals temporal requirements for the oscillating transcription factor NHR-23/NR1F1 in *C. elegans* larval progression. *bioRxiv* https://doi.org/10.1101/2021.10.27.465992 [PREPRINT]

Joost S, Zeisel A, Jacob T, Sun X, La Manno G, Lonnerberg P, Linnarsson S, Kasper M (2016) Single-cell transcriptomics reveals that differentiation and spatial signatures shape epidermal and hair follicle heterogeneity. *Cell Syst* 3: 221–237

Joost S, Annusver K, Jacob T, Sun X, Dalessandri T, Sivan U, Sequeira I, Sandberg R, Kasper M (2020) The molecular anatomy of mouse skin during hair growth and rest. *Cell Stem Cell* 26: 441–457

Kamath RS, Fraser AG, Dong Y, Poulin G, Durbin R, Gotta M, Kanapin A, Le Bot N, Moreno S, Sohrmann M *et al* (2003) Systematic functional analysis of the *Caenorhabditis elegans* genome using RNAi. *Nature* 421: 231–237

Katic I, Xu L, Ciosk R (2015) CRISPR/Cas9 genome editing in *Caenorhabditis elegans*: evaluation of templates for homology-mediated repair and Knock-ins by homology-independent DNA repair. *G3 (Bethesda)* 5: 1649–1656

Kim DH, Grün D, van Oudenaarden A (2013) Dampening of expression oscillations by synchronous regulation of a microRNA and its target. *Nat Genet* 45: 1337–1344

Kingma D, Ba J (2015) Adam: a method for stochastic optimization. In *3rd international conference for learning representations (San Diego)*, pp 1–13. http://arxiv.org/abs/1412.6980

Koike N, Yoo SH, Huang HC, Kumar V, Lee C, Kim TK, Takahashi JS (2012) Transcriptional architecture and chromatin landscape of the core circadian clock in mammals. *Science* 338: 349–354

Kostrouchova M, Krause M, Kostrouch Z, Rall JE (1998) CHR3: a *Caenorhabditis elegans* orphan nuclear hormone receptor required for proper epidermal development and molting. *Development* 125: 1617–1626

Kostrouchova M, Krause M, Kostrouch Z, Rall JE (2001) Nuclear hormone receptor CHR3 is a critical regulator of all four larval molts of the nematode *Caenorhabditis elegans*. *Proc Natl Acad Sci U S A* 98: 7360–7365

Kouns NA, Nakielna J, Behensky F, Krause MW, Kostrouch Z, Kostrouchova M (2011) NHR-23 dependent collagen and hedgehog-related genes required for molting. *Biochem Biophys Res Commun* 413: 515–520

Machlab D, Burger L, Soneson C, Rijli FM, Schubeler D, Stadler MB (2022) monaLisa: an R/Bioconductor package for identifying regulatory motifs. *Bioinformatics* 38: 2624–2625

Magnusdottir E, Kalachikov S, Mizukoshi K, Savitsky D, Ishida-Yamamoto A, Panteleyev AA, Calame K (2007) Epidermal terminal differentiation depends on B lymphocyte-induced maturation protein-1. *Proc Natl Acad Sci U S A* 104: 14988–14993

Meeuse MWM, Hauser YP, Hendriks G-J, Eglinger J, Bogaarts G, Tsiairis C, Großhans H (2020) Developmental function and state transitions of a gene expression oscillator in *C. elegans*. *Mol Syst Biol* 16: e9498

Menet JS, Rodriguez J, Abruzzi KC, Rosbash M (2012) Nascent-Seq reveals novel features of mouse circadian transcriptional regulation. *Elife* 1: e00011

Meng J, Ma X, Tao H, Jin X, Witvliet D, Mitchell J, Zhu M, Dong MQ, Zhen M, Jin Y *et al* (2017) Myrf ER-bound transcription factors Drive *C. elegans* synaptic plasticity via cleavage-dependent nuclear translocation. *Dev Cell* 41: 180–194

Miki TS, Carl SH, Großhans H (2017) Two distinct transcription termination modes dictated by promoters. *Genes Dev* 31: 1870–1879

Monsalve GC, Frand AR (2012) Toward a unified model of developmental timing: a "molting" approach. *Worm* 1: 221–230

Nüsslein-Volhard C, Wieschaus E, Kluding H (1984) Mutations affecting the pattern of the larval cuticle in *Drosophila melanogaster*: I. zygotic loci on the second chromosome. *Wilhelm Roux's Arch Dev Biol* 193: 267–282

Olmedo M, Geibel M, Artal-Sanz M, Merrow M (2015) A high-throughput method for the analysis of larval developmental phenotypes in *Caenorhabditis elegans. Genetics* 201: 443–448

Ou Q, King-Jones K (2013) What goes up must come down: transcription factors have their say in making ecdysone pulses. *Curr Top Dev Biol* 103: 35–71

Patel R, Galagali H, Kim JK, Frand AR (2022) Feedback between a retinoid-related nuclear receptor and the let-7 microRNAs controls the pace and number of molting cycles in *C. elegans. Elife* 11: e80010

Patke A, Young MW, Axelrod S (2020) Molecular mechanisms and physiological importance of circadian rhythms. *Nat Rev Mol Cell Biol* 21: 67–84

Paus R, Foitzik K (2004) In search of the "hair cycle clock": a guided tour. *Differentiation* 72: 489–511

Plikus MV, Van Spyk EN, Pham K, Geyfman M, Kumar V, Takahashi JS, Andersen B (2015) The circadian clock in skin: implications for adult stem cells, tissue regeneration, cancer, aging, and immunity. *J Biol Rhythms* 30: 163–182

Preußner M, Goldammer G, Neumann A, Haltenhof T, Rautenstrauch P, Müller-McNicoll M, Heyd F (2017) Body temperature cycles control rhythmic alternative splicing in mammals. *Mol Cell* 67: 433–446.e4

Pujol N, Cypowyj S, Ziegler K, Millet A, Astrain A, Goncharov A, Jin Y, Chisholm AD, Ewbank JJ (2008) Distinct innate immune responses to infection and wounding in the *C. elegans* epidermis. *Curr Biol* 18: 481–489

Ronneberger O, Fischer P, Brox T (2015) U-net: convolutional networks for biomedical image segmentation. In *Medical Image Computing and Computer-Assisted Intervention – MICCAI 2015*, Navab N, Hornegger J, Wells WM, Frangi AF (eds), pp 234–241. Cham: Springer International Publishing

Rual JF, Ceron J, Koreth J, Hao T, Nicot AS, Hirozane-Kishikawa T, Vandenhaute J, Orkin SH, Hill DE, van den Heuvel S *et al* (2004) Toward improving *Caenorhabditis elegans* phenome mapping with an ORFeome-based RNAi library. *Genome Res* 14: 2162–2168

Russel S, Frand AR, Ruvkun G (2011) Regulation of the *C. elegans* molt by pqn-47. *Dev Biol* 360: 297–309

Sandhu A, Badal D, Sheokand R, Tyagi S, Singh V (2021) Specific collagens maintain the cuticle permeability barrier in *Caenorhabditis elegans. Genetics* 217: iyaa047

Sefer E, Kleyman M, Bar-Joseph Z (2016) Tradeoffs between dense and replicate sampling strategies for high-throughput time series experiments. *Cell Syst* 3: 35–42

Singh RN, Sulston JE (1978) Some observations on molting in *Caenorhabditis elegans. Nematologica* 24: 63–71

Stec N, Doerfel K, Hills-Muckey K, Ettorre VM, Ercan S, Keil W, Hammell CM (2021) An epigenetic priming mechanism mediated by nutrient sensing regulates transcriptional output during *C. elegans* development. *Curr Biol* 31: 809–826

Steinmayr M, Andre E, Conquet F, Rondi-Reig L, Delhaye-Bouchaud N, Auclair N, Daniel H, Crepel F, Mariani J, Sotelo C *et al* (1998) Staggerer phenotype in retinoid-related orphan receptor alpha-deficient mice. *Proc Natl Acad Sci U S A* 95: 3960–3965

Stiernagle T (2005) Maintenance of *C. elegans. WormBook* https://doi.org/10.1895/wormbook.1.101.1

Stojanovski K, Großhans H, Towbin BD (2022) Coupling of growth rate and developmental tempo reduces body size heterogeneity in *C. elegans. Nat Commun* 13: 3132

Sundararajan V, Pang QY, Choolani M, Huang RY (2020) Spotlight on the granules (Grainyhead-like proteins) – from an evolutionary conserved controller of epithelial trait to pioneering the chromatin landscape. *Front Mol Biosci* 7: 213

Tabara H, Sarkissian M, Kelly WG, Fleenor J, Grishok A, Timmons L, Fire A, Mello CC (1999) The rde-1 gene, RNA interference, and transposon silencing in *C. elegans. Cell* 99: 123–132

Telerman SB, Rognoni E, Sequeira I, Pisco AO, Lichtenberger BM, Culley OJ, Viswanathan P, Driskell RR, Watt FM (2017) Dermal Blimp1 acts downstream of epidermal TGFbeta and Wnt/beta-catenin to regulate hair follicle formation and growth. *J Invest Dermatol* 137: 2270–2281

Thorvaldsdottir H, Robinson JT, Mesirov JP (2013) Integrative genomics viewer (IGV): high-performance genomics data visualization and exploration. *Brief Bioinform* 14: 178–192

Tsiairis C, Großhans H (2021) Gene expression oscillations in *C. elegans* underlie a new developmental clock. *Curr Top Dev Biol* 144: 19–43

Turek M, Bringmann H (2014) Gene expression changes of *Caenorhabditis elegans* larvae during molting and sleep-like lethargus. *PLoS One* 9: e113269

Turek M, Besseling J, Bringmann H (2015) Agarose microchambers for long-term calcium imaging of *Caenorhabditis elegans. J Vis Exp* 100: e52742

Venkatesan K, McManus HR, Mello CC, Smith TF, Hansen U (2003) Functional conservation between members of an ancient duplicated transcription factor family, LSF/Grainyhead. *Nucleic Acids Res* 31: 4304–4316

Wilanowski T, Caddy J, Ting SB, Hislop NR, Cerruti L, Auden A, Zhao LL, Asquith S, Ellis S, Sinclair R *et al* (2008) Perturbed desmosomal cadherin expression in grainy head-like 1-null mice. *EMBO J* 27: 886–897

Yang J, Fong HT, Xie Z, Tan JW, Inoue T (2015) Direct and positive regulation of *Caenorhabditis elegans* bed-3 by PRDM1/BLIMP1 ortholog BLMP-1. *Biochim Biophys Acta* 1849: 1229–1236

Yu Z, Lin KK, Bhandari A, Spencer JA, Xu X, Wang N, Lu Z, Gill GN, Roop DR, Wertz P *et al* (2006) The Grainyhead-like epithelial transactivator Get-1/Grhl3 regulates epidermal terminal differentiation and interacts functionally with LMO4. *Dev Biol* 299: 122–136

Yushkevich PA, Piven J, Hazlett HC, Smith RG, Ho S, Gee JC, Gerig G (2006) User-guided 3D active contour segmentation of anatomical structures: significantly improved efficiency and reliability. *Neuroimage* 31: 1116–1128

Zhang Y, Liu T, Meyer CA, Eeckhoute J, Johnson DS, Bernstein BE, Nusbaum C, Myers RM, Brown M, Li W *et al* (2008) Model-based analysis of ChIP-Seq (MACS). *Genome Biol* 9: R137

Zhang L, Ward JD, Cheng Z, Dernburg AF (2015) The auxin-inducible degradation (AID) system enables versatile conditional protein depletion in *C. elegans. Development* 142: 4374–4384